

Electronic Thesis and Dissertation Repository

---

5-12-2016 12:00 AM

## Ultra-High Field Strength MR Image-Guided Robotic Needle Delivery Device for In-Bore Small Animal Interventions

Matthew J. Gravett  
*The University of Western Ontario*

Supervisor  
Aaron Fenster  
*The University of Western Ontario*

Graduate Program in Biomedical Engineering  
A thesis submitted in partial fulfillment of the requirements for the degree in Master of Engineering Science  
© Matthew J. Gravett 2016

Follow this and additional works at: <https://ir.lib.uwo.ca/etd>



Part of the [Biomedical Devices and Instrumentation Commons](#)

---

### Recommended Citation

Gravett, Matthew J., "Ultra-High Field Strength MR Image-Guided Robotic Needle Delivery Device for In-Bore Small Animal Interventions" (2016). *Electronic Thesis and Dissertation Repository*. 3766.  
<https://ir.lib.uwo.ca/etd/3766>

This Dissertation/Thesis is brought to you for free and open access by Scholarship@Western. It has been accepted for inclusion in Electronic Thesis and Dissertation Repository by an authorized administrator of Scholarship@Western. For more information, please contact [wlsadmin@uwo.ca](mailto:wlsadmin@uwo.ca).

# Abstract

Current methods of accurate soft tissue injections in small animals are prone to many sources of error. Although efforts have been made to improve the accuracy of needle deliveries, none of the efforts have provided accurate soft tissue references. An MR image-guided robot was designed to function inside the bore of a 9.4T MR scanner to accurately deliver needles to locations within the mouse brain. The robot was designed to have no noticeable negative effects on the image quality and was localized in the MR images through the use of an MR image visible fiducial. The robot was mechanically calibrated and subsequently validated in an image-guided phantom experiment, where the mean needle targeting accuracy and needle trajectory accuracy were calculated to be  $178 \pm 54\mu\text{m}$  and  $0.27 \pm 0.65^\circ$ , respectively. Finally, the device successfully demonstrated an image-guided needle targeting procedure *in situ*.

## Key Words

image-guided intervention, medical robotics, needle delivery, ultra-high field strength magnetic resonance imaging, in-bore, preclinical, minimally invasive

# Co-Authorship Statement

Chapter two is being prepared for submission to Medical Physics, where the authors list is as follows: Matthew Gravett, Jeremy Cepek and Aaron Fenster. I designed, assembled and calibrated the robot, the electronics and the software, and performed the experiments describe in this thesis, including the mechanical force/torque and kinematic calculations, including FEA, the CMM testing, the in phantom MR image-guided needle targeting validation, and the mouse brain targeting experiment. Jeremy Cepek's contributions to this work involved advising me regarding the mechanical and electronic design, and he also wrote the majority of the PIC microprocessor code. Jeremy also helped with the aspects of the robotic system's design pertaining to MR compatibility. Kevin Barker was very helpful with mechanical design advice and calibration, and Jacques Montreuil machined parts for the robot. The work in this thesis was performed under the supervision of Aaron Fenster.

Dedicated to my parents and Baka

# Acknowledgments

I would like to acknowledge the contributions of many others in the development of this project.

I would like to start by thanking Dr. Fenster and Dr. Jeremy Cepek for their valuable guidance, insight and motivation throughout this project. I would also like to thank my advisory committee members, Dr. Drangova and Dr. Lacefield, for their advice and guidance.

I would like to thank Kevin Barker for his expert help and advice with design ideation and mechanical calibrations, and Jacques Montreuil for highly skilled machining of parts. I would like to thank Attica Manufacturing, specifically Brent Jesney, for letting us use their private CMM, and Leo Bourdeau for performing the measurements with the CMM.

I would like to thank Alex Li for his advice and help integrating the device into the 9.4T MR scanner, and Miranda Bellyou for her advice regarding the robot's mouse bed design and help performing the *in situ* demonstration. I would also like to thank Kyle Gilbert for the custom RF Coil design, as well as his insight into the effects of robot integration with the 9.4T MR scanner.

I would like to thank John Moore for his help 3D printing components and with PVA molding, and Golafsoun Ameri for her help molding the PVA phantoms.

Finally, I would like to acknowledge my sources of personal funding during the course of my degree: an Ontario Graduate Scholarship and a Western Research Graduate Scholarship, and project funding from the Ontario Institute for Cancer Research.

# List of Acronyms

2D	Two-dimensional
3D	Three-dimensional
AD	Alzheimer's disease
ALS	Amyotrophic lateral sclerosis
BBB	Blood brain barrier
CAD	Computer-aided design
CMM	Coordinate measuring machine
CNS	Central nervous system
CSF	Cerebrospinal fluid
DC	Direct current
DoF	Degree of freedom
DoFs	Degrees of freedom
EU	European Union
FDM	Fused Deposition Modelling
FEA	Finite Element Analysis
fMRI	Functional Magnetic Resonance Imaging
FoV	Field-of-view
FUS	Focused Ultrasound

HFU	High-frequency ultrasound
iMRI	Intraoperative magnetic resonance imaging
micro-CT	Micro-computer tomography
micro-PAT	Micro-photoacoustic tomography
micro-PET	Micro-positron emission tomography
micro-SPECT	Micro-single photon emission computer tomography
MR	Magnetic Resonance
MRI	Magnetic Resonance Imaging
N	Newton
PEEK	Polyetheretherketone
PVA	Polyvinyl alcohol
RCM	Remote center of motion
RF	Radio frequency
RoM	Range of motion
T	Tesla
TE	Echo time
TR	Repetition time
TRE	Total registration error
USA	United States of America

# Table of Contents

Abstract.....	i
Key Words.....	i
Co-Authorship Statement.....	ii
Acknowledgments.....	iv
List of Acronyms.....	v
Table of Contents.....	vii
List of Tables.....	x
List of Figures.....	xi
Chapter 1.....	1
1 Introduction.....	1
1.1 Preclinical Studies.....	1
1.2 Preclinical Medical Imaging.....	2
1.3 Preclinical Interventions.....	4
1.3.1 Minimally Invasive Interventions.....	4
1.3.2 Intraoperative Image-Guided Preclinical Interventions.....	6
1.3.3 Intraoperative Image-Guided Preclinical Robotic Interventions.....	7
1.4 Drawbacks of Current Preclinical Robotic Systems.....	10
1.5 Magnetic Resonance Imaging.....	12
1.6 Preclinical Applications.....	13
1.7 Preclinical Robot Workflow.....	14
1.7.1 Preclinical Image-Guided Robot Design.....	14
1.7.2 Mechanical Calibration.....	17
1.7.3 Robot Registration.....	17
1.8 Technical Objectives.....	19
1.9 Outline of Thesis.....	20
1.9.1 Chapter 2: The Design of an Ultra-High Field Strength MR Image-Guided Robotic Needle Delivery Device for In-Bore Small Animal Interventions.....	20
1.9.2 Chapter 3: Experimental Methods and Results in the Development of an Ultra-High Field Strength MR Image-Guided Robotic Needle Delivery Device for In-Bore Small Animal Interventions.....	20
Chapter 2.....	22



2	The Design of an Ultra-High Field Strength MR Image-Guided Robotic Needle Delivery Device for In-Bore Small Animal Interventions.....	22
2.1	Introduction .....	22
2.2	Robotic Design Methodology.....	26
2.2.1	MR Compatibility and Actuation Methods .....	26
2.2.2	In-Bore vs. Out-of-Bore Robot .....	27
2.2.3	Robotic Design Orientation.....	28
2.2.4	Needle Manipulator Design Methodology .....	29
2.2.5	Needle Driver Design Methodology.....	30
2.2.6	Needle Selection .....	31
2.2.7	Mouse Bed Manipulator Design Methodology.....	31
2.2.8	Mouse Bed Design Methodology.....	32
2.3	MR Image Guided Needle Delivery Robot Design .....	33
2.3.1	Needle Driver Design .....	33
2.3.2	Needle Manipulator Linkage Design .....	35
2.3.3	Mouse Bed Manipulator Design .....	39
2.4	Mechatronic System Design.....	41
2.5	9.4T MR Scanner .....	42
2.5.1	Radio Frequency Receiver Coil.....	42
2.6	Robot to MR Registration .....	43
2.6.1	Cross-Fiducial Design .....	43
2.6.2	MR to Robot Registration Process .....	44
	Chapter 3.....	46
3	Experimental Methods and Results in the Development of an Ultra-High Field Strength MR Image-Guided Robotic Needle Delivery Device for In-Bore Small Animal Interventions .....	46
3.1	Experimental Methods.....	46
3.1.1	Effects of the Robot on MR Images .....	46
3.1.1.1	Robot Induced Magnetic Field Distortion.....	47
3.1.1.2	Effect of the Robot on the Noise .....	48
3.1.2	Calibration and Accuracy Experiments .....	49
3.1.2.1	Open-Air Robotic Calibration and Accuracy Validation .....	49
3.1.2.2	Hydraulic Needle Driver Needle Length Calibration .....	52
3.1.2.3	Image Validation of Needle Accuracy in Phantoms .....	52
3.1.3	Total Image-Guided Needle Accuracy Validation in Phantom Tissue.....	54

3.1.4	<i>In Situ</i> Needle Delivery Accuracy Validation .....	54
3.2	Results .....	56
3.2.1	Open-Air Calibration and Accuracy Testing .....	56
3.2.2	Needle Tip Accuracy in Phantom Tissue .....	57
3.2.3	<i>In Situ</i> Preclinical Application.....	58
3.3	Discussion.....	59
3.3.1	Effects of the Robot on MR Images .....	59
3.3.2	Open-Air Calibration and Accuracy Testing .....	60
3.3.3	Needle Targeting Accuracy in Phantom Tissue.....	63
3.3.4	<i>In Situ</i> Preclinical Application.....	64
3.4	Conclusion.....	64
Chapter 4.....		66
4	Summary and Future Work.....	66
4.1	Summary .....	66
4.1.1	Chapter 2: The Design of an Ultra-High Field Strength MR Image-Guided Robotic Needle Delivery Device for In-Bore Small Animal Interventions .....	66
4.1.2	Chapter 3: Experimental Methods and Results in the Development of an Ultra-High Field Strength MR Image-Guided Robotic Needle Delivery Device for In-Bore Small Animal Interventions .....	67
4.2	Conclusion.....	68
4.3	Future Work.....	69
4.3.1	Mechanical Design Improvements .....	69
4.3.2	Controller Improvements.....	72
4.3.2.1	Electronic Improvements.....	72
4.3.2.2	Software Improvements .....	72
4.3.3	Registration Procedure .....	73
4.4	Final Remarks .....	73
References .....		75
Appendix .....		81
Appendix 1 .....		81
Curriculum Vitae .....		82

# List of Tables

Table 1: Table of all of the needle targeting and trajectory accuracies measured using a CMM and MR images .....	56
Table 2: The effect of needle angle on needle targeting and trajectory accuracy .....	61
Table 3: The non-linear relationship between encoder step size and the change in needle trajectory angle when the needle is tilted back, vertical and tilted forward .....	61

# List of Figures

Figure 1: CAD model render of the robot .....	33
Figure 2: Cross-section CAD model view of the hydraulic needle driver with the needle (a) retracted, and (b) extended .....	34
Figure 3: CAD model view of (a) the spherical linkage, (b) a cross-sectional view to illustrate the spherical linkage driving mechanism and (c) the aspherical linkage's range of motion .....	36
Figure 4: Spherical linkage 3D kinematic diagram .....	38
Figure 5: CAD model view of the mouse bed manipulator's (a) XYZ-stage, and (b) the Z-stage wedge mechanism .....	40
Figure 6: (a) Picture of the RF coil and (b) CAD model renders of the RF coil's orientation on the mouse bed, relative to the mouse brain and cross-fiducial .....	43
Figure 7: Graph of the RF signals measured in the MR scanner's bore with the robot inside the bore and powered .....	49
Figure 8: (a) CAD model view of the robot retrofitted with tooling balls used as known points on the robot's DoFs during CMM measurements, and (b) a picture of the CMM probe measuring the RCM tooling ball .....	51
Figure 9: Picture of the mouse taped to the robot's mouse bed with the RF coil placed over top of it for the <i>in situ</i> needle targeting demonstration .....	55
Figure 10: Plotted needle trajectories from the phantom tissue experiment (left), showing the needle trajectories converging at the RCM, and a magnified view of the needle trajectories relative to the RCM (right) .....	58

Figure 11: Axial MR images of the mouse’s brain (a) before needle insertion and (b) while the  
needle was inserted into the mouse’s brain ..... 59

Appendix 1: Solidworks FEA of the mouse bed model with a simulated applied load from the  
needle during a needle insertion ..... 81

# Chapter 1

## 1 Introduction

### 1.1 Preclinical Studies

Preclinical testing and validation is an essential step in the development of new and improved medical treatments. Products ranging from pharmaceuticals to surgical devices must endure demanding pre-clinical testing to prove their validity for human trials. According to the World Health Organization, the global pharmaceutical market value is \$300 billion per year and is continuously rising, with companies investing two-thirds of their revenue on research and development. Mice account for over 60% of the animals used for experimental purposes in the European Union (EU) in 2011<sup>1</sup>. Assuming that the proportions of animal classes are similar between the EU and the United States of America (USA), there are at least 8.6 million mice used for experimental purposes annually in the USA alone<sup>2</sup>. Mice are an ideal testing model since their genetic and biological characteristics are similar to humans, but also because they are inexpensive to purchase, feed and house, and require little space to store.

Genetically modified mice have played an extensive role in preclinical research of human diseases since 75% of mice genes are orthologous in humans and can be genetically engineered to carry genes to model human diseases<sup>3</sup>. The two most common genetically modified mice are knockout mice and transgenic mice. Knockout mice are engineered by deactivating specific genes, while transgenic mice have specific genes replaced with another gene to characterize the effects of the specific genes on preclinical experiments. Knockout and transgenic mice are used in the research of virtually every disease, such as a variety of cancers<sup>4,5</sup>, and neurodegenerative diseases such as Alzheimer's disease (AD)<sup>6,7</sup> and amyotrophic lateral sclerosis (ALS)<sup>6,8</sup>, to name a few.

Mice in the pharmaceutical market are a prime patient model for determining the market readiness of a drug. Preclinical drug toxicology experimentation in mice is generally conducted over a 6-12 month period to determine long-term toxicology effects, while a lifetime exposure study in mice provides the carcinogenic effects of the drug<sup>9</sup>. Drugs that were successful in treating knockout mice were correlated to selling well in the market<sup>10</sup>. Although knockout and transgenic mice are invaluable to the development of disease and disorder treatment, they cost up to a thousand times more than standard lab mice.

## 1.2 Preclinical Medical Imaging

The field of preclinical medical imaging plays a significant role in the quantification of preclinical study results, and has nurtured the development of new fields of preclinical imaging research. The development of new and improved imaging modalities benefits both the medical industry with advanced imaging technologies for diagnosis while benefitting the preclinical industry with high-quality research tools. The most common non-invasive small animal imaging modalities are high-frequency ultrasound (HFU), micro-computed tomography (micro-CT) and magnetic resonance imaging (MRI), while there is also research interest in micro-photoacoustic tomography (micro-PAT), micro-positron emission tomography (micro-PET) and micro-single photon emission computer tomography (micro-SPECT).

The current generation of high-frequency ultrasound scanners are compact, ergonomic and capable of real-time high resolution 2D imaging at up to 400 frames per second<sup>11</sup>, and can be equipped with 3D array probes, making HFU a versatile tool for small animal researchers. While most imaging modalities, such as micro-CT and MRI, are not portable, ultrasound machines are portable and the transducers are easily manipulated by the user, facilitating the acquisition of images. This is especially useful when performing manual percutaneous interventions. HFU scanners are relatively inexpensive compared to other imaging modalities, and therefore more

accessible to researchers. The disadvantages of ultrasound imaging in general is the inability to image through bone and gases (air in the lungs), vulnerability to a wide variety of image artifacts and poor contrast resolution, while HFU, more specifically, is limited to shallow penetration depths. For example, a frequency of 50MHz can achieve an imaging resolution in the axial and lateral directions of 20 $\mu$ m and 100 $\mu$ m respectively; however, the maximum penetration depth at that resolution would be about 8-9mm<sup>12</sup>.

The development of micro-CT scanners has yielded amazing benefits for preclinical imaging, with applications in orthopedic and vascular research. Current small animal micro-CT scanners possess 3D imaging capabilities at an isotropic voxel size of 150 $\mu$ m within a matter of seconds<sup>13</sup>. The desired imaging resolution directly increases the scan time, and since more X-rays projections are required to form the image, radiation exposure is higher in longer scans. Long scans are therefore commonly used for specimen imaging and can achieve an isotropic voxel size of 30 $\mu$ m using geometric magnification<sup>14</sup>. Micro-CT image contrast is dependent on the attenuation of X-rays, which requires imaging samples to be electron dense or have high atomic number elements; therefore, micro-CT imaging is better suited for preclinical orthopedic imaging research. Although inherent soft tissue contrast resolution in micro-CT is poor, contrast aided imaging of vascular structures is an effective technique to visualize the cardiovascular system, especially tumor vasculature.

Magnetic resonance imaging (MRI) has emerged as a powerful diagnostic tool and has been continuously improved since its inception. The chief benefit of MRI is the capability of high-resolution 3D imaging with high-soft tissue contrast. These imaging capabilities are beneficial to preclinical neuroimaging research since the living brain can be studied in more detail than ever before, which opens the opportunity for new studies to produce new information on mechanisms in healthy, disease and disordered brains. Current research aims at improving image quality and overall patient care by developing new techniques for a variety of applications to more accurately



quantify MR image data. The development of ultra-high magnetic field strength superconducting magnets has led to increases in sensitivity, contrast, and imaging resolution, which facilitate the improvement and development of imaging techniques, such as high resolution imaging<sup>15</sup>, perfusion and functional imaging (fMRI)<sup>15,16</sup> and spectroscopy<sup>15</sup>. These MR imaging techniques are key in observing and analyzing the development and treatment of animal models with brain diseases; for example neurodegenerative diseases like AD and ALS.

## 1.3 Preclinical Interventions

Preclinical interventions are an essential part of preclinical testing for new medical technologies, as it is often the first time that these technologies are tested in *in vivo* subjects. The complexity of preclinical interventions ranges from relatively simple tail vein injection, to complex mouse hip replacements and lung transplants<sup>17</sup>. This dissertation will focus on local needle interventions in mice.

### 1.3.1 Minimally Invasive Interventions

Many common interventional procedures in humans typically requiring surgical exposure have been redesigned for minimal invasiveness through surgical planning techniques and tools; such as laparoscopic appendectomy, nephrectomy, heart valve replacements. The fundamental ideology behind minimally invasive interventions is that less trauma during surgery results in faster healing and lower risk of morbidity<sup>18,19</sup>. The same is true in preclinical models, such as mice. Many research techniques require invasive surgical exposure of the injection site in order to perform local injections of drugs or cells in specific organs or tumors. This highly invasive surgical procedure induces trauma in the mouse resulting in pain and distress, and in turn result in the impact of uncontrolled factors in the study, such as morbidity and mortality<sup>20,21</sup>. The high dependency on the preclinical surgeon for unaided manual injection accuracy adds to the potential for human error in the study. Since the goal of preclinical studies is a controlled and repetitive mouse model, the

induction of trauma on a test subject is an undesired dependent variable, as the trauma is a result of conducting the experiment and not a part of the mechanism under study.

Stereotaxy is a widely used technique for guiding brain interventions in both humans and animals. Stereotactic interventions are limited to intracranial procedures since the target coordinates are derived from skull geometries paired with mouse brain atlas coordinates. Although stereotaxic instruments can deliver mechanical positioning accuracies anywhere from 100 $\mu$ m to 1 $\mu$ m, the relevant accuracy is dependent on the quality of the reference atlas. As discussed in Section 1.1, genetically modified mice have proven to be a vital tool in preclinical research; however, the wide variety of strains have a wide variety of neuroanatomical differences, including brain proportions, which in-turn decreases considerably the stereotaxic accuracy<sup>22-24</sup>. With neuroanatomical proportion differences and scaling functions based on mouse size, it is difficult to determine accuracy of stereotaxic targeting<sup>25</sup>. Other limitations of mouse brain atlases include lack of detailed neonatal atlases, the potential for inaccuracy during tissue sectioning and fixation of brain pathology slices, and the limited number of slice orientations available, which increases the difficulty of designing oblique needle paths to avoid damaging sensitive neuroanatomical structures<sup>25</sup>. Recently, pre-operative MR and micro-CT images have been combined with pathology slices to create more accurate reference atlases<sup>26</sup>.

Pre-operative images are often used as reference for planning minimally invasive interventions in humans. A common example in humans is the use of pre-operative MR and CT images for stereotactic brain surgery, with intraoperative fluoroscopic imaging. The images are used to safely plan the optimal path through the brain to reach the target, as opposed to relying on the outdated method of using brain atlases, which are based off approximate anatomical locations and are not patient specific.

### 1.3.2 Intraoperative Image-Guided Preclinical Interventions

Non-invasive intraoperative image-guidance is a fundamental tool that has enabled the success of minimally invasive surgeries. The numerous benefits of minimally invasive surgeries include eliminating the need for surgical exposure of the target, reducing the risk of morbidity, as well as the length of recovery, and in turn decreasing hospital costs. Visualization through intraoperative image-guidance of the target and surrounding anatomy allows surgeons to ensure surgical accuracy through immediate image verification. After the patient is closed, post-operative imaging of a surgical site is performed to verify that the surgery was successful. In some cases, the images determine that the surgery was not completely successful and the patient requires a second intervention. The capability of postoperative, pre-closing, imaging of the surgical target allows the surgeon to ensure the procedure was successful during the surgery, reducing the likelihood of another surgery. Ultrasound is arguably the most commonly used non-invasive imaging modality for interventional image-guidance since ultrasound systems are relatively inexpensive compared to a micro CT or MR scanner.

Free-hand ultrasound guided injections are often performed in mice since it is convenient to hold the ultrasound probe in one hand and insert needle with other hand while using the US image as real-time position reference<sup>21,27</sup>. Micro-CT and MR image-guided preclinical interventions are more challenging than ultrasound guided procedures due to spatial constraints of the imaging modalities. Although the imaging field of view (FoV) is accessible by hand in some micro-CT scanners, the user cannot insert a needle under image-guidance due to ionizing radiation exposure, hence micro-CT scanners are often equipped with a lead shielded housing. The FoV in the preclinical MR scanners is practically inaccessible since it can be located up to a meter into the MR scanner's bore, and the gradient inserts for mouse imaging have a bore diameter from 90mm<sup>28</sup> to 120mm (9.4T MR scanner at Robarts Research Institute). For human applications, intraoperative

MRI (iMRI) scanners were developed to allow neurosurgeons direct access to the patient's head<sup>29</sup>. The first iMRI systems, like the open "double doughnut" magnet system used a low main magnetic field strength, limiting the imaging resolution but allowed surgeon access to the patient from above and from the sides<sup>29</sup>. Although the 'double doughnut' MR scanner design would accommodate the presence of a preclinical surgeon for MR image-guided interventions, the scanner's low magnetic field design would be incapable of high-resolution imaging, along with other imaging features. Even if it were possible to perform a manual MR image-guided injection in small animals, some sort of alignment/stereotactic mechanism would be required since the target is so small, and the 10 $\mu$ m needle tip diameter is extremely fragile and could unintentionally break off in the mouse with minimal torque applied to the needle while inserted.

Overall, the current line of high-resolution imaging modalities cannot be modified for manual image-guided interventions without consequence. The spatial constraints and presence of ionizing radiation in micro-CT hinders the potential for manual interventions with intraoperative image-guidance, while the redesign of preclinical MR scanners to better accommodate image-guided interventions would undo the technological advancements towards ultra-high magnetic field strength imaging. Therefore, image guided interventions using micro-CT or MRI require an alternative solution, such as robotic interventions.

### 1.3.3 Intraoperative Image-Guided Preclinical Robotic Interventions

It is clear that the development and use of robotics has transformed many industries, a prime example being the manufacturing industry. Robots are reliable, accurate, low maintenance and can generally perform the same tasks as trained workers more efficiently, without a loss in quality. Fatigue and working conditions are not of concern to robots as the electric motors actuating the robots can run for thousands of hours. The design of a robot can be tailored to a specific task or

procedure. Surgical robots are especially suitable for minimally invasive image-guided interventions since the size of the end-effector and end-effector manipulator can be minimized, resulting in less crowded surgical area and a more dexterous end-effector. Depending on the application, the dexterity of the end-effector manipulator's design could incorporate more or fewer DoFs and range of motion than a surgeon is capable of providing.

Image-guided robotics not only boast benefits of image-guidance and minimally invasive interventions, robotic devices also reduce the intervention's sensitivity to human error. Hospital error during surgical procedures in the operating room accounts for between 40-50% of all reported cases<sup>30</sup>. To reduce the potential for human error, the neuroArm MR image-guided robotic surgical device used for human brain surgeries employs the use of software to create "no go zones". These zones delineated in the MR images as delicate areas of the brain, causing the software to prevent the motors from moving the robot's arms to those positions<sup>31</sup>. Robotic surgical devices can be designed with extremely fine position encoding, resulting in finer end-effector motion than is capable by a skilled surgeon<sup>32</sup>. As discussed in Section 1.3.2, image-guided interventions increase surgical accuracy, therefore, the combination of these two image-guidance and robotic surgical tool manipulation ought to considerably improve surgical accuracy, and greatly benefit the overall clinical outcome.

Preclinical research has already been impacted by the use of image-guided robotics used for HFU and micro-CT image-guided needle deliveries in mice<sup>13,33,34</sup>. A robotically manipulated linkage with motorized needle insertion was designed and validated for HFU image-guided needle delivery and a needle positioning accuracy of <100 $\mu$ m and a total registration accuracy (TRE) of 145 $\mu$ m under HFU guidance<sup>35</sup>. This same device was adapted to perform out-of-bore intraoperative image-guided injections, since the robot is too large to fit inside the micro-CT scanner bore and the mouse is unable to be imaged during the needle delivery procedure. The micro-CT version achieved

a stated TRE of  $198 \pm 18\mu\text{m}$ <sup>35</sup>. The most advanced version of a micro-CT image-guided robot used a six DoF robot to perform in-bore needle insertions into mice with an accuracy of  $149 \pm 41\mu\text{m}$ <sup>13</sup>.

As discussed in Section 1.2, micro-CT imaging has unique advantages in terms of fast, high-resolution, imaging; however, there are many benefits of non-invasive medical imaging with high-soft tissue contrast for experimental validation. Preclinical ultra-high field strength MR scanners also boast many unique imaging techniques, in part due to the high-spatial resolution. The MR image-guided human surgical robotics field has had numerous efforts to develop MR image-guided surgical robotic tools to improve on a variety of surgical procedures ranging from prostate ablation<sup>36</sup> to stereotactic based glioma resection<sup>32</sup>. The field of image-guided robotic interventions for micro-CT scanners has had many more developments than the field of preclinical MRI, with only a few published efforts. *E. Wilson et al.* developed an out-of-bore, 3 linear DoF, 7T MR image-guided robotic device to perform brain biopsies in mice with a targeting accuracy of 1mm<sup>37</sup>.

Penetration of the blood brain barrier (BBB) is the sole natural transport path between the systemic blood flow and the cerebrospinal fluid (CSF). The BBB is formed by brain endothelial cells that filter out certain substances while carrying blood to the cerebrospinal tissue. For over a decade, studies have proven that the use of focused ultrasound (FUS) applied to blood flow immersed with microbubbles can disrupt the BBB and temporarily allow the passage of larger molecules<sup>38</sup>. Studies have determined the appropriate frequency and pulse pattern, in conjunction with ultrasound microbubble-contrast agent, to allow larger molecules to pass the BBB with negligible side effects. This principle led to the development of an MR image-guided FUS device for BBB disruption in rodent brain models where an MR compatible FUS probe is controlled to emit the FUS pulses to a specific area of the brain.

## 1.4 Drawbacks of Current Preclinical Robotic Systems

Considering the development of the field of preclinical medical imaging, there have been relatively few attempts to develop an MR image-guided robot for preclinical needle delivery. As medical imaging technology and quality improve, researchers will require devices with higher accuracy to perform interventions in small animals. This effect has been observed in human surgeries with the MR image-guided stereotactic neurosurgical robot, neuroArm. Preclinical researchers perform a wide variety of injections on small animals as part of preclinical testing of drugs and disease treatments, many of which are performed in soft tissues, which are optimally imaged by MRI.

The HFU image-guided robot discussed in Section 1.3.3 provides many advantages to minimally invasive needle insertion since HFU machines are readily available, easy to use and impose minimal spatial constraints. Limitations of these systems lie mainly in the nature of the imaging modalities' inability to provide high-contrast resolution and shallow scan depth of <1cm at high frequencies. In certain applications, such as intracranial injections, the HFU transducer requires space on the mouse's head, limiting the insertion site area and trajectory possibilities during needle insertion. The in-bore micro-CT image-guided robot developed by *Bax et al* achieved high functionality and robustness for needle delivery. A limitation of this device is that it is equipped with a metal needle, which can cause CT image artifacts, hence reducing the quality of the images acquired with the inserted needle. As with the HFU robot, the main limitation of this system is the inability to visualize soft tissues throughout the procedures, which is useful for target selection, needle tip targeting verification and the ability to perform MRI specific imaging techniques. This micro-CT image-guided robotic device is also considerably larger than the preclinical MR scanner bore and is not MR compatible in terms of materials and electronics.

The out-of-bore MR image-guided robot developed by *Emmanuel et al* was intended for tissue biopsy, and has a very low mean targeting accuracy of approximately 1/5<sup>th</sup> of what is considered acceptable for performing biopsies on specific regions of the brain using high resolution image guidance of structures including small tumors<sup>39</sup>. Another limitation of this device is its inability to perform the biopsy inside the MR scanner bore where it would be able to image the inserted needle and discern whether the needle tip is at the tumor site. This device is also limited to vertical needle trajectories, implying that a new burr hole is required for every new biopsy, unless the target is close to the initial biopsy needle axis. The linearly constrained needle trajectory inhibits the angulation of the needle, which is useful when avoiding sensitive areas of the brain<sup>25</sup>. This device employs a combination of image and mechanical registration, in which a point selected in the MR images defines the origin of the MR coordinate system while relying on mechanical alignment of the coordinate system axes. The simplicity of this registration method most likely is reflected in the device's low targeting accuracy, especially considering that this device has a relatively simple design, incorporating the positioning error of only three linear DoFs, as opposed to other devices with upwards of six DoFs (including rotational DoFs).

As previously discussed, the FUS BBB disruption device for preclinical MR image-guidance shows promising results as a minimally invasive method of allowing high molecular weight molecules to pass through the BBB to regions of the brain. The major benefit of this procedure is that it is non-invasive, requiring simply a caudal vein injection of ultrasound contrast microbubbles accompanied by the agent that is intended to cross the BBB, virtually eliminating the impact of trauma on the experimental rodent model. This technology has a promising future but is currently lacking some fundamental capabilities. This device uses a focused ultrasound beam, which has a full width at half maximum impact volume of  $1.2 \times 1.2 \times 6.6 \pm 0.1 \text{mm}^3$ , meaning that injected agent is able to disperse into many regions of the brain<sup>28</sup>. The robotic positioning accuracy of 0.5mm means that the impact volume could miss up to almost 50% of the intended target volume.



A substantial amount of drugs, cells or other agents needs to be systemically injected to treat neurological diseases and disorders since most of the injected material is removed by the renal system, resulting in a suboptimal concentration of the material in the CSF; local injection assures the delivery of therapeutic material at a regulated concentration<sup>40</sup>. There is an increase in the vulnerability of the brain to unwelcome material since there is no specific mechanism that selects what can, or cannot, pass through the BBB using this technique, leading to potential misinterpreted experimental results, or other more serious effects on the small animal. The applications of this technique are also limited to brain therapies. For this technology to transfer into humans at its current state of development, the patient requires a partial craniotomy since ultrasound does not transmit well through the human skull, unlike thin mouse skulls.

## 1.5 Magnetic Resonance Imaging

The most important advantage that MRI possesses over CT imaging is safety. CT scanners are incapable of being completely harmless since the inherent imaging property involves the use of ionizing radiation. Therefore, patient safety in the use of CT imaging involves decreasing the radiation dose per scan. The major drawback of MR imaging is due to the long scan times. Over time, technological advances may permit the development of highly sensitive antennas, requiring fewer averages and therefore faster scans.

Although many metal implants are non-ferromagnetic, such as dental implants, hip and knee replacements and electronic implants like pacemaker and cochlear implants, they still pose imaging artifact issues<sup>41,42</sup>. MRI sequence improvements have aided in reducing artifacts caused by scanning patients with metal implants, but this issue is not completely solved<sup>43,44</sup>. With perpetual improvements of MRI over the past few decades, across various applications, it is evident that is still untapped potential.

## 1.6 Preclinical Applications

An ultra-high field strength MR image-guided robot would serve as a useful tool to overcome preclinical needle targeting errors in soft tissues. An example of a preclinical procedure requiring the use of accurate MR image-guided needle delivery robot is in the study of cerebral vasospasm in subarachnoid hemorrhage. Controlled vasospasms can be induced by performing autologous blood injections into the cisterna magna to help identify and mechanisms contributing to vascular pathology linked with subarachnoid hemorrhage. Current methods require the dissection of the occipital muscles from the occipital bone to expose the atlanto-occipital membrane, which is then punctured by a needle to inject the autologous blood at the cisterna magna<sup>45,46</sup>. These injection are technically demanding and laborious, and also induce trauma on the mice<sup>46</sup>. An MR image-guided robotic device should serve to remove the tedious surgical process and provide high targeting accuracy. Alternatively, while current methods evaluate pathology slices 24 hours after the procedure, performing the procedure under MR image-guidance would provide the researcher with various vascular imaging techniques which could help quantify the injection, as well as the immediate effects of the study<sup>46</sup>.

There are currently preclinical research experiments that require high needle targeting accuracies than the conventional stereotactic methods. A study currently being performed by a group in our brain research lab involves the use of stereotactic injections into a specific area of the hippocampus. The stereotactic arrangement's accuracy is not high enough to perform accurate and repeatable injections, and therefore, the majority of the injections are not being performed at the desired target. This is an ideal case where an MR image-guided robotic device would serve to enhance the needle targeting accuracy for a preclinical study.

Another preclinical application for an MR image-guided needle delivery device involves monitoring the interstitial fluid pressure in mouse tumor using the wick-in-needle technique, as

performed using the micro-CT compatible device developed by Bax et al<sup>13</sup>. However, since micro-CT has low soft tissue contrast, the tumors require contrast to visualize the target tumor, unlike MRI, since it has superior soft tissue contrast.

## 1.7 Preclinical Robot Workflow

### 1.7.1 Preclinical Image-Guided Robot Design

Unlike conventional surgeries where the surgeon uses ergonomic, handheld, tools to enhance their dexterity and range of motion, medical robots are generally purpose built, allowing developers to create custom robotic designs, catering to the specific surgeries. A common feature among surgical robotic design is the use of a remote center of motion (RCM), which uses a mechanical linkage to pivot an end-effector about a fixed point in space called the “fulcrum”. Mechanically, the fulcrum is the point in space where the axes of the four arm links coincide (see illustration in Fig. 3(a) in Section 2.2.1.2). Depending on the robotic application, the design of the RCM device can be active or passive. Thus, a controlled RCM can be induced through software so that the robot’s arms pivot the end-effector about the RCM (active), or by using a mechanical linkage design that inherently pivots about an RCM (passive). In surgical applications, the active RCM of the end-effector that enters the patient’s body can be located at its entry point into the body, actively ensuring that the motion of the robotic arms and end-effector does not move relative to the surgical entry point, therefore minimizing the surgical entry incision and hence patient trauma. This principle was similarly applied in the development of the preclinical micro-CT image-guided device by *Waspe et al* which used a passive RCM linkage with a position controlled needle driver<sup>47</sup>. A passive RCM linkage is calibrated so that the needle trajectory passes through the RCM; however, error is introduced by inserting the needle passed through the calibrated RCM since the needle angle error begins contributing to the targeting accuracy of the procedure.

A key detail that defines the image-guided device is whether it is an in-bore or out-of-bore device and how the device will be positioned relative to the scanner during the procedure. Most micro-CT scanners have a motorized animal “couch” used to insert and retract the small animal from the micro-CT scanner’s bore. The “couch” is an ideal mechanism for the robotic integration as it allows for easy pre-interventional setup and also accommodates the design of a robot where the entire device does not need to fit inside the imaging bore. Preclinical MR scanners generally have a gradient coil bore diameter of <120mm with the imaging FoV located up to 1 meter into the bore, whereas the micro-CT FoV begins only a few centimeters into the bore. With the FoV at a much further distance into the bore of preclinical MR scanners compared to micro-CT scanners, it is not ideal to use an out-of-bore based MR image-guided robot since it would require the end-effector to be mounted on the end of a long arm to reach the FoV. Such a long arm would likely introduce error in the targeting accuracy and require a substantial amount of power to manipulate if it were unsupported. Unlike human MR scanners, preclinical MR scanners do not have a motorized patient bed, which raises particular difficulties regarding device integration. The imaging bores in micro-CT and preclinical MR scanners are spatially limited and become more limited with the introduction of a robotic manipulator. The current hand-held preclinical surgical tools are intended to be held by human hands, and they are therefore designed to be relatively large in order to accommodate the natural dexterity of the surgeon. It is likely necessary to redesign the end-effectors to conform with the spatial requirements of the image-guided robotic device, in terms of shrinking and eliminating features that only benefit human use.

It is vital that an image-guided robotic device has limited effect on the modality’s image quality. If the device is intended for real-time image guidance (in-bore device), then the materials present in the imaging FoV cannot have an effect on the image quality, such as image artifacts introduced by imaging metal components in ultrasound, micro-CT and MRI. Apart from designing a robot that can physically fit inside the bore of a micro-CT scanner and prevent robot induced

image artifacts, there are no major factors that can affect micro-CT image-guided procedures. The design of in-bore MR image-guided devices have to overcome additional constraints.

Conventional electric motors like DC stepper motors, cannot be used in the magnetic environment since they operate based on induced magnetic fields. This has led engineers to test alternative actuation methods for MR compatible robots for human procedures, including pneumatic, hydraulic and piezoelectric stepper motors, leading to successful results<sup>48-52</sup>. Although components for pneumatic and hydraulic actuation can be made from MR compatible materials and can exert large forces, their positional accuracy is too low, >1 mm, for preclinical applications requiring micron accuracy<sup>48,50</sup>. Piezoelectric motors are much more compact than pneumatic or hydraulic actuators and are capable of sub-nanometer step resolution. Unlike DC stepper motors, piezoelectric stepper motors use piezoelectric ceramic element resonance to microscopically step the motor's output shaft. These motors come in compact linear and rotary configurations, are backlash free, and have an intrinsic holding force equal to the maximum output force, even while the motors are not powered. The piezoelectric motors are predominantly composed of metal and hence need to be kept at a certain distance away from the MR scanner's FoV in order to prevent magnetic field distortion, resulting in image distortion and therefore position localization error.

Device electronics can be sensitive to radio-frequency pulses emitted by the MR scanner and need to be properly shielded to prevent the induction of noise in the motor and encoder signals. Another important electronic design consideration is the effect of the signal from the system electronics on the MRI system, which uses radiofrequency (RF) emissions from the imaged sample for spatial encoding. Most clinical research MR scanners have low-pass filters built into the wall between the control room and the MR suite to filter outside RF signals from the device electronics, which could interfere with the resonance frequency of the MR scanner.

## 1.7.2 Mechanical Calibration

Proper calibration of any robotic device is an important step to ensure its accuracy and repeatability. The method of calibration is dependent on the robot design. Many surgical robot designs employ the use of a passive RCM linkage, where the end-effector (in this case a needle) pivots about the spherical linkage's RCM. Since the end-effector pivots about the RCM, this linkage design decouples the motion of the linkage arms from the positional accuracy of the needle. Thus, in a properly calibrated passive spherical linkage, the needle tip position does not change, regardless of the change in position of the needle arms.

A common method of calibration used in the development of some RCM based micro-CT image-guided needle delivery robots involves the use of a camera to photograph the needle through a set of predetermined positions in two perpendicular planes, repeated along each of the rotational axes. Needle axis and tip segmentation performed on the images determines the needle targeting error and in-plane needle angle error. This calibration method is relatively simple but only applicable if the end-effector is located in front of the device and the camera's viewing angle is unobstructed by other parts of the device<sup>53</sup>.

An alternative method of mechanical calibration involves the use of a coordinate measuring machine (CMM), which uses a highly accurate mechanical probe to measure physical geometry. These machines are often used to measure machined parts as a method of quality control but can also be used to calibrate mechanical devices by adding temporary tooling balls to the end-effector<sup>54</sup>. The position of the tooling ball centroids, and hence the end-effector, are measured by the probe over a number of positions and compared to the kinematic predictions.

## 1.7.3 Robot Registration

Registration refers to the transformation of a point in one coordinate system into another. For image-guided interventions, in order to use an imaging modality as reference to guide a robotic

medical device, the relative positions of the imaging system and the robotic device must be known. Depending on the physical features of the imaging modality, a mechanical or image registration method can be implemented to localize the robot relative to the image coordinates. Ideally, image guided robotic devices would be mechanically fixed/coupled with the imaging modality, allowing the immediate commencement of the procedure. Mechanical registration can be difficult to develop since there can be bed reattachment errors and most clinical scanners are not designed to accommodate image guided robotic devices<sup>34</sup>. Image based device registration is often performed by identifying the position of known fiducial geometries of the robot in images, and relating those positions to the imaging modality's coordinate system.

The fiducial selection should be done carefully since the localization of the fiducial in the images directly relates to the overall accuracy of the device. The device's coordinate system can be defined by a minimum of three fiducial points from the images. Since micro-CT images are formed through X-ray attenuation, a fiducial can be made from radio-opaque material for high fiducial contrast. In micro-CT, this simply requires one 3D image acquisition of the fiducial located at a known position on the device. The quantification of consistent geometric accuracy of a micro-CT scanner used for position localization is also important due to inter-scanner variability.

Fiducial localization in MR is more complex since position localization is dependent on the magnetic field homogeneity, which is sensitive to the introduction of foreign materials in the magnetic field, and therefore variable. A study performed by *Cepek et al* compared the effects of geometric distortion of the static magnetic field on the fiducial localization error of three passive fiducial designs<sup>55</sup>. This study concludes that the use of a "cross shaped" fiducial composed of water, for higher contrast, can be imaged so that fiducial localization is insensitive to both slice select and in-plane error. This method requires image sets of the fiducial acquired in two perpendicular planes with one of the axes oriented perpendicularly to the slice select planes. These two image sets need to be re-acquired but with the frequency encoding directions swapped in order to eliminate the in-

plane error due to magnetic field inhomogeneities. The “cross-fiducial” registration method is ideal since it has a simple fiducial design with a robust localization technique. The drawback of this registration, and MRI in general, is that MR images take a long time to acquire compared to micro-CT images. For example, a 3D image of an entire mouse with an isotropic voxel size  $\sim 150 \mu\text{m}$  can be acquired in  $\sim 16$  seconds with a GE eXplore micro-CT scanner, while a 3D image with an isotropic voxel size of  $150 \mu\text{m}$  of only a mouse brain requires a 30 minute acquisition with a 9.4T Agilent preclinical MR scanner<sup>13</sup>. Therefore, a quick method of device registration would be beneficial to the integration of MR image-guided devices into preclinical and clinical settings.

## 1.8 Technical Objectives

The objective of this research is to advance the quality of preclinical needle deliveries in soft tissue by providing a reliable and accurate robotic tool, guided by ultra-high field strength MR images. The device must be able to deliver needles to the targets throughout the volume of the mouse brain, at a mean targeting of  $<200\mu\text{m}$  in order to accurately target the smallest clinically relevant pathologies, and angulate the needle with a mean trajectory accuracy of  $<1^\circ$  to avoid sensitive structures. The entire device must be small enough to be placed inside the MR scanner’s bore and its mechanical and electrical components must have a limited effect on the geometric accuracy and quality of the MR images. The device must be user friendly and make the procedure more efficient than the current manual methods. Proof-of-concept must be validated through device to MR registration, characterization of positioning errors and to demonstrate capabilities in phantom and *in-situ* experiments.



## **1.9 Outline of Thesis**

### **1.9.1 Chapter 2: The Design of an Ultra-High Field Strength MR Image-Guided Robotic Needle Delivery Device for In-Bore Small Animal Interventions**

This chapter describes the robotic design methodology based on the unique constraints of the MR environment. The robot's mechanical design is tailored to preserve the scanner's magnetic field homogeneity, function within the spatial constraints of the MR scanner's bore, maximize the targeting volume and needle trajectory range of motion and employ high-precision design features. Custom electronics were designed to communicate with the large number of encoders used to control the motor positions and control the robot based on the derived kinematic equations. Finally, a passive robot to MR registration method insensitive to magnetic field inhomogeneity is described using an MR visible fiducial imbedded in the robot's mouse bed.

### **1.9.2 Chapter 3: Experimental Methods and Results in the Development of an Ultra-High Field Strength MR Image-Guided Robotic Needle Delivery Device for In-Bore Small Animal Interventions**

This chapter describes the methods employed to develop and validate an MR image-guided robotic needle delivery device for small animals. The mechanical device calibration and in-air needle targeting accuracy was determined through CMM measurements. The device was used to deliver needles to virtual targets in phantom tissue to determine the total accuracy of the device

using MR images. Finally, an experiment was conducted to validate the device's capabilities in a realistic experimental situation by inserting a needle into the mouse brain.

# Chapter 2

## 2 The Design of an Ultra-High Field Strength MR Image-Guided Robotic Needle Delivery Device for In-Bore Small Animal Interventions

### 2.1 Introduction

Many pre-clinical research techniques require accurate local injections of cells, drugs, genes or contrast agents to specified targets in small animals, such as mice<sup>21,56-61</sup>. Previous success has been demonstrated with micro-CT<sup>13,34</sup> and ultrasound image-guided robotic devices<sup>33</sup>, designed to accurately deliver needles to specific sites in mice, however, there has not been a complete solution for accurate needle delivery in the bore of an MR scanner.

Pre-clinical minimally invasive interventional procedures performed on rodents offer major advantages over invasive surgical techniques in terms of the effect of trauma to the mouse, and the effect of trauma on its immune system, which risks compromising the experimental outcome<sup>20</sup>. Many research practices require accurate, minimally invasive, local injections to specific sites in mice, for example: cancer therapies in the brain<sup>56</sup>, mammary gland<sup>57</sup> and pancreas<sup>58</sup>; stem cell therapies in the heart<sup>21</sup> and spinal cord<sup>59</sup>, as well as gene therapy in the thymus gland<sup>60</sup> and spinal cord<sup>61</sup>, to name a few. Manual subcutaneous implantation of cells (xenograft) is a

common method for researchers to grow cells *in vivo* which does not require highly accurate needle targeting. However, a minimally invasive orthotopic xenograft injection, requiring cells from a specific organ to be accurately transplanted into the same organ of another species, provides a better representation of the original microenvironment, but requires high accuracy needle targeting in tissues. Therefore, this procedure requires an accurate injection to the desired site in the organ. Our research institute has a highly developed small animal brain-imaging group; therefore, in these works we focus on brain injections in mice.

Intravenous bolus injections in mice are commonly performed via the caudal vein; however, the BBB limits access of some compounds to the central nervous system (CNS) using this injection site<sup>62,63</sup>. Due to this and other limitations, many pre-clinical research studies require accurate injection of cells, drugs or contrast agent into precise locations in the brains of mice<sup>24,64-66</sup>. Currently, these injections are performed using a stereotactic device with an atlas for reference, or a blind injection by hand with only external anatomical reference such as skull features. Either of these techniques can result in the inaccurate placement of needles due to human error, and may require multiple attempts for a successful insertion. These inaccurate insertions may result in failed experiments and fatality for the mice. If the injection is successful, an MR image may be used to monitor the effects of the injection on local tissues or the distribution/migration of the contrast agent throughout the brain, which is optimally observed immediately after injection. Due to the time it takes to prepare the mouse for imaging, and performing the MR imaging pre-scanning procedures, the concentration of contrast agent in the blood may be reduced by an unacceptable amount before imaging<sup>67</sup>. To help circumvent this issue, mice are often sacrificed after injection so that injected dyes or contrast agents will remain in their system for imaging<sup>68,69</sup>. However, sacrificing these mice inhibits the observation of the long term effects of the experiments, and can also be expensive if the mice have genetic variations, especially if the sacrifice fails to yield acceptable imaging results and needs to be repeated.

The field of image-guided robotic needle delivery in pre-clinical animal models has grown over the past decade. Robotically assisted micro-CT image guided out-of-bore<sup>34</sup> and in-bore<sup>13</sup> needle placement devices with <200 $\mu$ m mean accuracy have been successfully tested on mice. Despite this success, the level of soft tissue contrast achievable with MRI is not possible with CT, making MRI the preferred image modality for needle guidance in certain studies where soft tissue is being imaged (*e.g.*, those requiring intracranial injections).<sup>29</sup> The most advanced previous work focused on out-of-bore image guided percutaneous biopsy via a MRI-guided robotically assisted system guided by Bruker BioSpin 7T MR scanner images, which achieved a needle tip placement accuracy within 1mm in phantom experiments.<sup>37</sup> Apart from the low needle targeting accuracy and the fact that the system is currently only used for biopsy, and not injections, the major drawback to this system is the inability of immediate imaging after needle insertion, since the biopsy is performed outside of the bore, which would allow quantification of *in vivo* accuracy and effects of the procedure. Another disadvantage is that the needle can only be oriented vertically, requiring a new burr hole (manually drilled hole in the mouse's skull) for additional biopsies along other insertion axes, hence increasing the invasiveness of the procedure, and making insertions to multiple non-vertically aligned targets cumbersome to perform.

The ability to automatically deliver needles to multiple targets with the use of an accurately calibrated robotically actuated needle delivery robot through one burr hole in the skull inflicts less trauma on the mouse and eases the preparation workflow. Thus, a purpose of our robot is to improve mouse preparation workflow by reducing the number of burr holes needed to complete the injections. In addition, our goal is to deliver a needle while the mouse is inside the bore of an ultra-high field strength MR scanner, thereby allowing researchers to perform serial needle insertions accurately and efficiently, with the ability to observe the inserted needle tip location and evaluate the immediate effects of the injection.

Ultra-high field strength pre-clinical MRI scanners (*e.g.*, 9.4T systems) consist of long and narrow bores (~2m long and 12cm in diameter for our 9.4T system) with the imaging FoV inaccessible by the human arm for manual injections under MRI-guidance. Due to this limitation and the requirement for substantially greater accuracy and repeatability than achievable with manual insertion, a robotic system must be designed to fit in the MRI scanner bore and perform needle insertions and injections into a mouse brain with a targeting accuracy of <200 $\mu$ m to target the smallest biologically relevant targets such as vessels<sup>70</sup> or tumors,<sup>71</sup> and a trajectory accuracy of <1° to avoid damaging surrounding features in the brain and minimize the required size of burr hole. In addition, brain images in live mice are generally acquired at a resolution between 150-200 $\mu$ m (150 $\mu$ m isotropic voxel size for 3D imaging and 200  $\times$  200 $\mu$ m<sup>2</sup> in 2D with 500  $\mu$ m slice thickness), and therefore the robot should be able to accurately deliver a needle to a specific voxel. Higher resolution brain images can be acquired, but the imaging time increases linearly as the voxel volume decreases since more averages are needed in order to form an image with enough signal.

Conventional electric motors present a major challenge in the development of MRI-guided interventional robots since they operate using a generated magnetic field, which would be detrimental to the image quality if they were introduced into the MR scanner's bore. To circumvent this issue, MR compatible robotic devices have generally been actuated using pneumatics<sup>48,49,72,73</sup>, since conventional electric motors are not compatible with the magnetic environment. More recently, due to advancements in piezoelectric material technology, small MR compatible piezoelectric motors have become a practical actuation method by combining sub-nanometer step size with a relatively high holding force while unpowered. In human studies, piezoelectric motors were used to successfully actuate the intraoperative MRI-guided NeuroArm robot for neurosurgical procedures. Based on their advantages and proven capability in the magnetic environment, piezoelectric motor actuation was used in the development of an ultra-high-field MR-compatible image-guided needle delivery robot for minimally invasive procedures in mice.

This chapter describes our development of a six DoF ultra-high field strength MR image-guided, in-bore, minimally invasive robotic system used to place needles accurately and precisely into targets in a mouse brain. The needle target and trajectory are determined from the MR images and output to the mechatronic system to deliver the needle accurately. The robot's accuracy and precision was quantified using three separate tests, each accounting for sources of error. The open-air accuracy was characterized and the needle targeting and trajectory were further evaluated through image-guided needle targeting procedures in brain mimicking phantom tissue, and finally, an image-guided needle targeting procedure was performed *in situ* to demonstrate the utility of the system for ultra-high field strength MR image-guided neurosurgical procedures in mice.

## 2.2 Robotic Design Methodology

Many robot design iterations were performed and evaluated to yield this final design. The major mechanical design constraints stemming from the in-bore MR environment include MR compatibility, the spatial constraints of the MR scanner's bore and positional accuracy of the robot.

### 2.2.1 MR Compatibility and Actuation Methods

A common issue regarding MR compatible robotics involves the use of metal parts which degrade the MR image quality if the metal parts are too close to the imaging FoV. MR compatible robots must therefore be designed predominantly from plastic and composites which significantly reduces the strength of the entire robot. Piezoelectric motors provide the high positional resolution required for this robot and although their power is relatively weak compared to DC motors, mechanical features can be designed to minimize the required motor output force.

Robots are commonly actuated using DC stepper motors, however, these DC motors are often made from ferromagnetic materials and use magnetism to produce mechanical power. If introduced into the MR environment, the magnetic field of the MR scanner would act on the DC stepper motors and pull it into the MR scanner's bore, which would be catastrophic for the scanner,

the robot and the mouse. Pneumatic and hydraulic actuators are also used in MR compatible devices since their components can be manufactured from non-ferromagnetic metals and plastics. These actuators can provide high output forces, however, their positional accuracies are much too low (>1mm). Non-magnetic piezoelectric motors are offered in linear and rotary configurations, are simple to use, have an intrinsic holding force equivalent to the motor's output, and provide high resolution actuation making them ideal for MR compatible devices. The two major design constraints to overcome when dealing with piezoelectric motors involves their non-ferromagnetic metallic design, which can distort the scanner's magnetic field and therefore the images if the motor is too close to the imaging FoV, as well as the low output force which may require an intermediate mechanical mechanism to reduce the output force required from the motors. The piezoelectric motors used for this robot were also selected due to their compact design, and provide sufficient speed to move the robot's DoFs over their RoM within a few seconds.

## 2.2.2 In-Bore vs. Out-of-Bore Robot

The robot was designed to be used with the Agilent 9.4T MR scanner which has a bore hole diameter of 12cm, with the imaging FoV at roughly 1m into the bore (the bore hole is ~1.5m above the ground). Initial design concepts included an out-of-bore robot, made up of a large moveable base with a long cantilevered arm used to insert needles into the mouse that was on a mouse bed at the imaging FoV. The difficulties posed with this design involve the long cantilevered arm, which would be subjected to a large moment under its own weight, causing bending and deflection of the cantilevered arm. This is more problematic considering the cantilevered arm would be made from plastic or composites, making it even more unstable. The deformation would directly impact the inaccuracy of the robot. In addition, an out-of-bore design prevents the RF shielding door from closing and shielding the bore hole, which would allow RF noise to enter the bore and could introduce noise into the MR images. Therefore, an in-bore robot would provide



more benefits than an out-of-bore robot, including smaller components and a smaller simple design, targeting accuracy, as well as RF shielding.

### 2.2.3 Robotic Design Orientation

Previous image-guided needle delivery robots had few, if any, spatial constraints. The image-guided robot developed by *Waspe et al.* was designed to be guided by ultrasound images, which does not pose any restrictions on the size of the robot. This robot was later used for micro-CT image-guided needle deliveries; however, the procedures were performed outside of the imaging bore since the robot was too large to perform the needle insertion in-bore. A micro-CT image guided robot was developed by *Bax et al.* to perform needle deliveries inside the micro-CT scanner's bore, however, only the needle manipulator linkage enters the imaging bore.

Both the ultrasound and micro-CT image-guided devices discussed use an RCM based needle manipulator, to angulate and insert the needle, while an XYZ-stage is used to translate the needle manipulator. These devices utilize six DoFs to perform the needle insertions, which is the minimum number of DoFs needed to perform needle deliveries to various targets in 3D, at various trajectories with independent needle insertion control.

The first CAD model prototypes of the in-bore MR image-guided robot used a similar design to the ultrasound and micro-CT image guided robots where the needle manipulator was mounted onto an XYZ-stage and the mouse was on a mouse bed that was connect to the base of the robot and where it's brain is at the MR scanner's isocenter. In this case, the robot and the mouse bed were mounted on a common base plate with an MR visible fiducial located in the mouse bed. The needle manipulator is too high when its mounted on top of the XYZ stage and is unable to reach the mouse brain, and the XYZ-stage can only be designed to be so small. An alternative design was considered where the needle manipulator linkage was cantilevered off of the XYZ-stage, however, the weight of the needle manipulator, needle driver and motors would create a

moment that would make the robot more prone to bending and deformation. Another issue with using the XYZ-stage to control the position of a canted needle manipulator is that the Z-stage needs to be able to lift the X- and Y-stages, as well as the needle manipulator, which would require substantial amount of force from the Z-stage motors to lift a long cantilevered arm. These issues were resolved by separating the XYZ-stage and the needle manipulator by mounting them on a common base plate; where the XYZ-stage is used to move the mouse bed, along with the MR visible fiducial which is embedded into the mouse bed, in three linear DoFs, while the needle manipulator is on the opposite side of the mouse, facing the XYZ-stage (see Fig. 1). Using the XYZ-stage to position the mouse requires a cantilevered mouse bed with a step down, which is designed to lower the position the mouse since the XYZ-stage is too tall to use as a mouse bed.

## 2.2.4 Needle Manipulator Design Methodology

An RCM is a desired feature in the design of the needle manipulator since it can be used to decouple the needle tip position from the needle angle. The ultrasound image-guided device discussed employs a 2D four-bar linkage mechanism to angulate the needle forwards and backwards, while the entire four bar linkage mechanism is rotated to angulate the needle side to side. The simplicity of this four-bar linkage design is beneficial to the overall needle targeting accuracy since there are fewer sources of mechanical error, such as additive tolerance errors. One of the difficulties of using this design for an MR compatible robot involves the close proximity of the metal four-bar linkage motor to the imaging FoV. The motor could be moved further away from the imaging FoV, using a belt to drive the linkage, however, this would require the motor to be mounted to an extension of the four-bar linkage base to allow it to tilt side to side with the four-bar linkage. The major issue with this design is that a large torque is required by the motor to tilt the weight of the four-bar linkage components that need to be rotated when the needle is tilted side to side, which would be too high for the relatively weak MR compatible piezoelectric motors. An alternative needle manipulator design using a spherical four bar linkage, like the one used in the

micro-CT image-guided robot previously discussed. This linkage design also requires two motors, however, the required torque to rotate the entire linkage is split between two motors, and in addition, the motors can control the linkage arms from a fixed position at a distance, through a pair of concentric shafts (see Fig. 3b). The spherical linkage design has a more limited range of motion than the 2D four-bar linkage, however, since the needle manipulator was removed from the XYZ-stage, the size of the spherical linkage can be maximized in order to utilize the full diameter of the MR scanner's bore. In addition, the bend in each arm joint was designed to be  $70^\circ$ , which allows the robot to provide the desired RoM of up to  $45^\circ$  from the vertical in all directions. If the needle manipulator were to be moved inside the mouse bed using the XYZ-stage as in previous designs, the spherical would need to be smaller as to not collide with the scanner's bore when being moved side to side or up by the XYZ-stage. A smaller spherical linkage also limits the range of needle angulation as well as the needle insertion depth.

## 2.2.5 Needle Driver Design Methodology

As previously discussed, the MR scanner's magnetic field is distorted by the presence of metal, including non-ferromagnetic metals such as aluminum, brass, titanium and tungsten. Since the needle driver is positioned directly above the imaging FoV, the use of the non-magnetic linear piezoelectric motors to insert and retract the needle would likely distort the magnetic field. The alternative actuation methods are hydraulic and pneumatic. Pneumatic actuation was avoided due to the need for an air compressor, vacuum, and a valve control system. Hydraulic actuation was selected for its relative simplicity since it was intended to be manually actuated using a syringe. Conventional hydraulic design uses two hydraulic chambers to move the hydraulic piston forwards and backwards with the full input force. Due to spatial constraints, a single chamber hydraulic actuator was integrated into the robot design, with the limitation being that the needle driver would rely on vacuum suction from the retraction of the syringe to retract the needle after the injection is performed. Furthermore, the needle driver's position must be known to ensure that the needle driver

is actuated to the desired depth to coincide with the RCM. This was overcome by designing hard stop which restricted the needle driver's range of motion to two positions: inserted and retracted.

## 2.2.6 Needle Selection

Mice are commonly injected using thin metal needles, however the presence of metal near the imaging FoV would likely induce image artifacts, affecting the image quality. Glass micropipettes seemed to be the most promising alternative to metal needles since glass is much stronger and less pliable than plastic. Conversely, glass is more brittle than plastic indicating that non-axial forces applied to the needle may cause it to bend/deflect and break. Needle deflection is common in beveled metal needles because the bevel acts as a rudder to steer the relatively flexible needle off of its intended trajectory. Glass micropipettes can have a diameter of roughly 1mm and can have a conical tip with a needle tip opening of around 10 microns in diameter. This conical tip would have very little contribution to needle deflection since it is symmetric, unlike the beveled metal needles.

## 2.2.7 Mouse Bed Manipulator Design Methodology

The mouse bed manipulator uses a set of three mechanical stages to move the mouse bed in three linear degrees of freedom. The mouse bed design uses a wedge mechanism which creates vertical motion by passing a wedge beneath another wedge that is constrained to moving in the vertical direction. To properly support the load distribution, each degree of freedom should use a pair of linear bearings. Non-magnetic linear slide bearings are commercially available, but come at an enormous financial cost, thus the search and development of an alternative linear rail bearing design was pursued. A simple rail bearing design using precision ground tungsten rods and precision ceramic ball bearings was used in this design, but at a fraction of the cost of non-magnetic slide rails. The design uses four tungsten rods to essentially form a cage around the ceramic ball bearings. One pair of tungsten rods are constrained, allowing one pair of rails to roll over the

ceramic ball bearings. Set screws are used to apply pressure to a titanium plate which is placed behind a pair of the rails to pre-load the bearing in order to remove any non-axial play in the bearing. Precision ground tungsten rods were used because of their smooth precision finish, which reduces friction, and tungsten is also harder than other non-ferromagnetic metals, and should prevent wearing. Ceramic ball bearings were used for their hardness and high spherical accuracy, which should provide accurate linear motion, and the smooth polished finish should also reduce friction. A linear stage was machined and tested to ensure the amount of friction induced by preloading the bearings.

The efforts made to reduce the weight lifted by the Z-stage were valuable, and even with the use of a wedge which reduced the required motor force by 43%, the Z-stage still required two motors to exert enough force to overcome the weight and linear bearing friction of the parts it was lifting.

## 2.2.8 Mouse Bed Design Methodology

The mouse bed is where the mouse is placed after being prepped for the injection procedure, and is moved in three linear degrees of freedom by the mouse bed manipulator. The Agilent 9.4T MR scanner does not have a body RF coil and due to spatial limitations, a custom RF coil was designed to be mounted on the mouse bed and fit tight around the mouse's head. The volume bounded by the RF coil defines the imaging FoV, which must encompass the mouse brain as well as the MR visible fiducial. The fiducial is made from a solid piece of plastic and therefore must be positioned within the RF coil volume without interfering with needle trajectories. The fiducial was therefore designed to be embedded into the mouse bed to ensure that it would not interfere with the mouse head position or large angle needle trajectories.

## 2.3 MR Image Guided Needle Delivery Robot Design

The small animal needle delivery robot consists of three main mechanical components (see Fig. 1): (1) the needle driver, (2) the spherical linkage, and (3) the XYZ-stage. The hydraulic needle driver inserts and retracts the needle tip to a fixed point in space, about which it is pivoted by the spherical linkage. The XYZ-stage moves the mouse bed until the desired needle target in the mouse brain is coincident with the fixed point in space about which the spherical linkage pivots, allowing the needle to be inserted to the target. All of these assemblies are fixed to a common base plate that is entirely inserted into the MR scanner's bore.

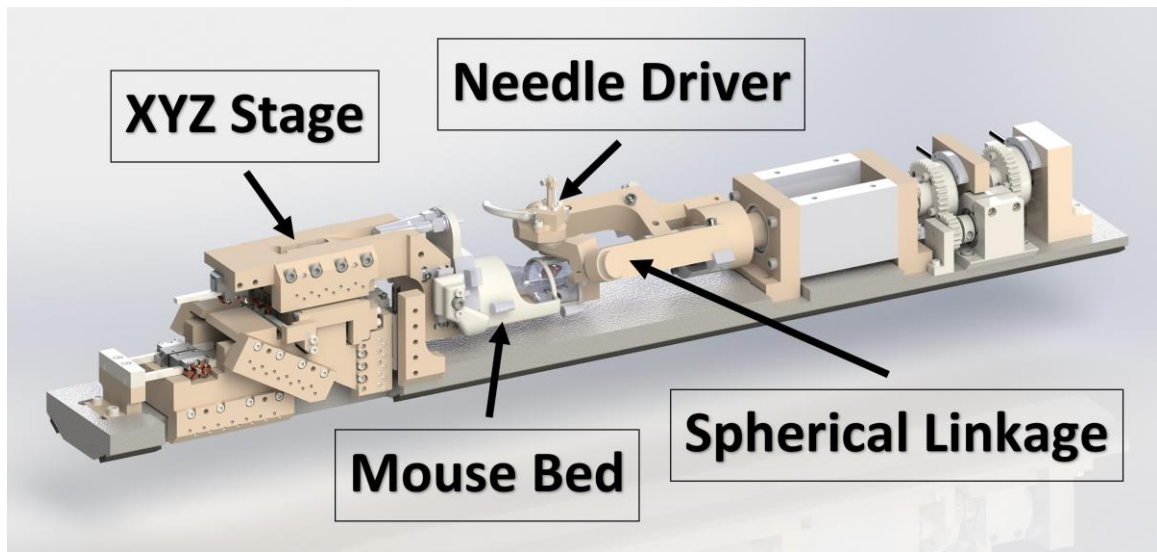


FIG. 1. CAD model rendering of the robot with the four main components labeled.

### 2.3.1 Needle Driver Design

Hydraulic actuation was selected to control the needle insertion and retraction during injection procedures. The needle driver is made up of a piston, which is actuated inside the hydraulic enclosure by the acting hydraulic fluid - water in our application. A needle guide and needle clamping mechanism are integrated into the piston design to align and fix the orientation of

the MR compatible glass needle (TIP10XV119, World Precision Instruments, Inc., Sarasota, FL) to the piston, in order to extend and retract the needle tip. The piston design also incorporates a precisely machined end-stop on the underside of the clamping mechanism, which allows for the needle length to be accurately calibrated to intersect with the RCM, which is explained in the following section (see Fig. 2).

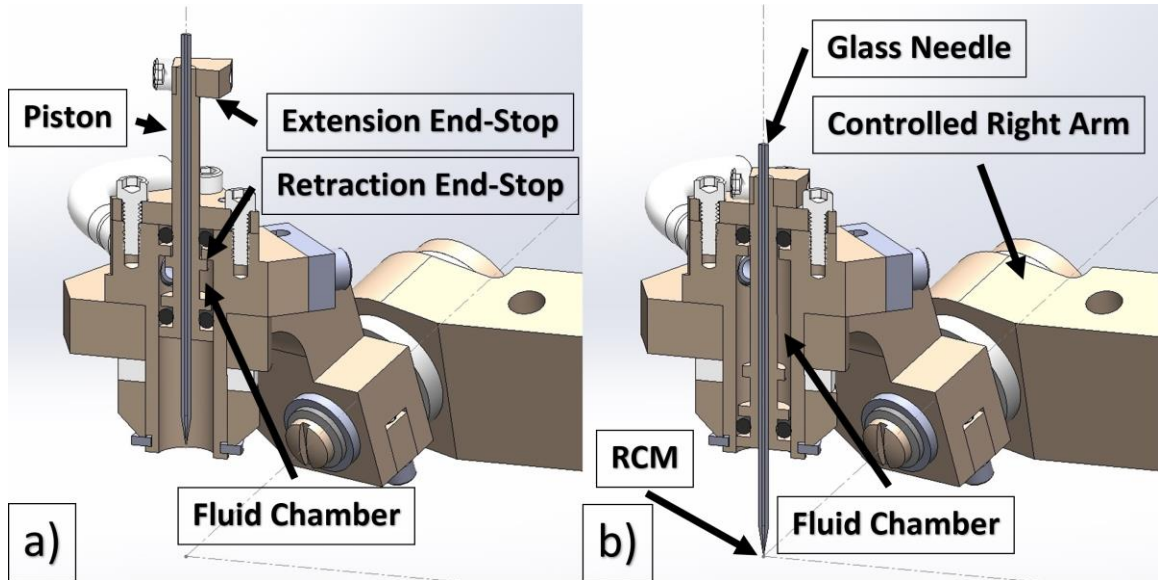


FIG. 2. A cross-section CAD model view of the hydraulic needle manipulator (a) retracted and (b) extended to each hard-stop. The needle tip is retracted into the hydraulic housing for clearance (a) while the linkage and mouse bed manipulator are being manipulated to prevent damage to the needle, and (b) the needle is then extended to the RCM during the needle delivery procedure.

The alternate approach of using MR compatible piezoelectric motors and optical encoders were not used for the needle driving system since they would be in close proximity to the imaging FoV, and the metallic components would cause image artifacts (metal induced artifacts in MR images is discussed later). The hydraulic system was therefore machined from polyethetherketone (PEEK) plastic instead of metal. PEEK was selected as the material of choice since it is one of the strongest non-composite plastics available. For simplicity, the hydraulic actuation was designed to be manually actuated using a syringe for this study and is intended to be automated in future. The syringe actuated hydraulic can easily output the necessary force to insert and retract the needle in tissues as well as allow the user to control the speed of the needle insertion and retraction.

## 2.3.2 Needle Manipulator Linkage Design

The hydraulic needle driver assembly is mounted on the end of the needle manipulator linkage and is used to control the trajectory of the needle.

The needle manipulator linkage employs a spherical four-bar linkage, which features a remote center-of-motion (RCM), about which the linkage joints pivot. The linkage consists of two controlled arms and two passive arms (see Fig. 3(a)). The needle driver is mounted in the joint between the two passive arms, where the protruding length of the needle is calibrated so when the hydraulic piston is extended to the end-stop, the needle tip is coincident with the RCM (see Figs. 2(b) and 3(a)). Mounting the hydraulic needle driver in the joint between the passive arms allows the linkage to manipulate the trajectory of the hydraulic needle driver to an angle of up to  $45^\circ$  from vertical and  $360^\circ$  about the vertical needle position, while maintaining the extended needle tip position at the RCM (see Fig. 3(c)). The needle's large angular range of motion (RoM) allows the robot to reach targets that have an obstructed line of sight.



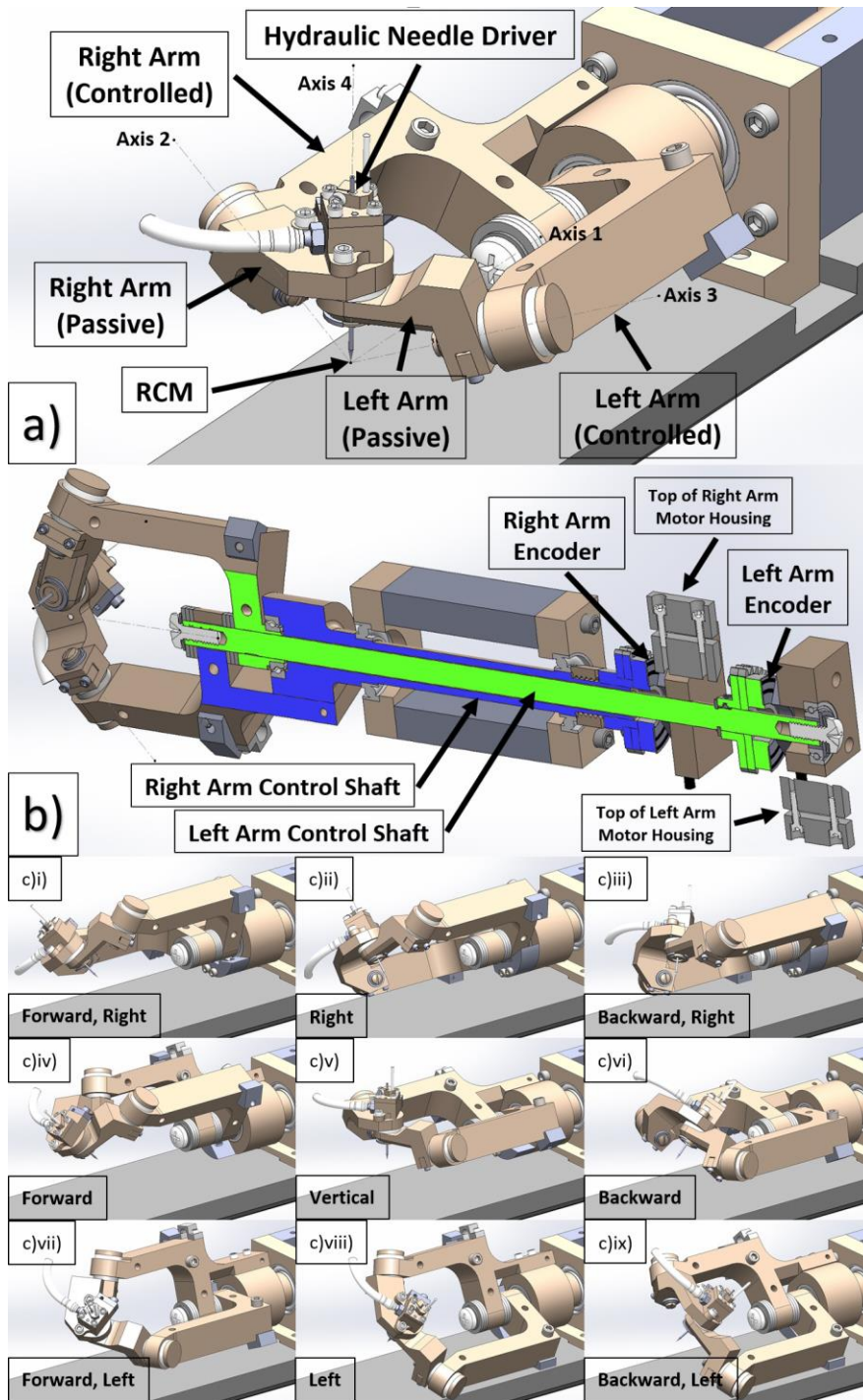


FIG. 3. A CAD model view of the spherical linkage system. (a) Linkage orientation and hydraulic needle driver mounting position within the mutual joint of the passive arms. Dotted lines illustrate the joint axes and the needle axis converging at the RCM. (b) Cross-section CAD model view from underneath the robot to visualize the concentric shafts that link the controlled linkage arms to the gears that are driven by the rotary stepper motor pinion gears (the motors and pinions are cut out of this cross-sectional view). The blue and green cross-section represents the components that drive the motion of the right and left controlled arms, respectively. (c) A CAD model of spherical linkage positioning the needle at a  $45^\circ$  angle (apart from c)v) at various trajectory angles to illustrate the linkage's RoM.

The controlled arms are mounted on long concentric shafts (Fig. 3(a)) to allow for independent control of each of the controlled linkage arms at a distance from the FoV, to avoid generating artifacts in the MR images due to the presence of the metallic motor. The MR compatible rotary piezoelectric stepper motors (LR5012D-00B10, PiezoMotor, Uppsala, Sweden) have a  $<0.057^\circ$  step angle and output torque of 55mNm, and their angular position is tracked using MR compatible, incremental, rotary optical encoders (RIK4-2C 29/1000 C03 9.0M Z, RS 29/16/1000, Numerik Jena, Jena, Germany) at a resolution of  $0.18^\circ$ . An anti-backlash preloaded gear is mounted on the far end of each of the two concentric shafts (see Fig. 3(b)) and each of the two anti-backlash gears are meshed with a pinion driven by a piezoelectric motor to gear-down the motor's output. Since the diameter of the gear is twice that of the pinion, the step resolution of each arm is doubled to  $0.09^\circ$  per step, and the effective output torque from the motors is doubled as well, to 110mNm. The linkage does not need to be counterbalanced since the stepper motors possess an intrinsic holding torque, even when unpowered. This intrinsic holding torque allows the motors to be turned off while maintaining the position of each degree-of-freedom. There is no electrical transmission from the motor driver to the motor when the motor is not moving. This is important in the MR environment because electrical signals travelling through wires near the scanner's FoV can cause image noise and other artifacts.

The inverse kinematics equations were derived to calculate the encoder positions for any desired needle trajectory using Napier's principle, as seen in Equations 1-6. The kinematic diagram of the linkage arm is illustrated in Figure 4.

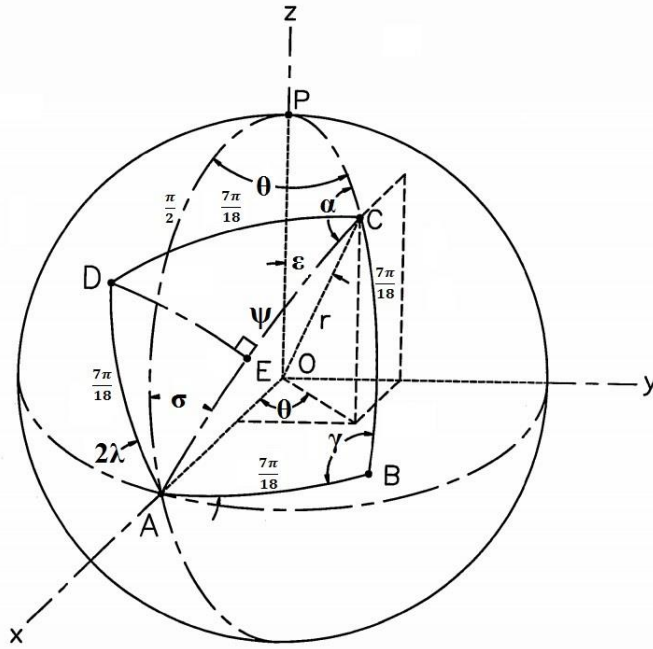


FIG. 4. 3D kinematic diagram of the spherical linkage with labelled kinematic variables. The segments A-B and A-D represent the controlled right and left linkage arms, respectively, while the segment B-C and D-C represent the passive right and left linkage arms, respectively. Each linkage arm has an angle of  $70^\circ$  ( $7\pi/18$  radians). The needle is represented by the segment C-O, which has length  $r$ . The angle between the Z-axis and the needle trajectory is represented by  $\epsilon$ , while the angle between the X-axis and the needle trajectory is represented by  $\psi$ . The angle between the passive and controlled arms is represented by  $\gamma$  (symmetric on the right and left side due to linkage geometry). The angle between the X-Z plane (APO) and the needle trajectory plane (CPO) is represented by  $\theta$ . Therefore, the angle between the controlled arms, represented by  $2\lambda$ , and the angle between the X-Z plane and the ACO plane, denoted by  $\sigma$ , can be determined through inverse kinematic calculations. The corresponding linkage joint axes between Figure 3(a) and Figure 4 are Axis 1 and the A-O (X-axis), Axis 2 and B-O, Axis 3 and D-O, and Axis 4 and C-O.

The right and left controlled arm angles are computed as a function of the needle trajectory, defined by the angles  $\epsilon$  and  $\theta$  through the inverse kinematics equations:

$$\psi = \cos^{-1}(\sin(\epsilon) \cdot \cos(\theta)) \quad (1)$$

$$\gamma = \cos^{-1} \left( \frac{\cos(\psi) - \cos^2\left(\frac{7\pi}{18}\right)}{\sin^2\left(\frac{7\pi}{18}\right)} \right) \quad (2)$$

$$\sigma = \cos^{-1} \left( \frac{\cos(\epsilon)}{\sin(\psi)} \right) \quad (3)$$

$$\lambda = \sin^{-1} \left( \frac{\sin\left(\frac{7\pi}{18}\right) \cdot \sin(\gamma)}{\sin(\psi)} \right) \quad (4)$$

$$\varphi_{Right\ Arm} = \sigma + \lambda \quad (5)$$

$$\varphi_{Left\ Arm} = \sigma - \lambda \quad (6)$$

Although this motorized spherical linkage provides controlled angulation of the needle about a fixed point, the capability of moving the RCM to multiple targets within a 3D volume is needed. This capability was provided by a separate linear three DoF XYZ-stage.

### 2.3.3 Mouse Bed Manipulator Design

The mouse bed manipulator consists of a three DoF linear stage with a cantilevered mouse bed oriented underneath the RCM linkage to maneuver the desired target inside the mouse brain to the RCM. The mouse bed manipulator can move  $\pm 12.5\text{mm}$  in the X- and Y-direction (along the length of the bore and side to side, respectively) and  $\pm 6.25\text{mm}$  in the Z direction (up and down), which is a sufficient working volume to target the entire mouse brain. The linear bearings of each linear stage are a custom-made ball-bar bearing design, in which four precision ground tungsten rods enclose a set of low diametric tolerance ceramic balls bearings. The linear bearings are preloaded from the side using a titanium plate to ensure even distribution of the preload along the titanium rods, intended to constrain the non-axial motion of the bearing. The X- and Y-stages are each composed of two sets of these bar-ball linear bearings and are actuated by MR compatible linear piezoelectric stepper motors (LL1011C-101A0A00, PiezoMotor, Uppsala, Sweden) at a  $<1\mu\text{m}$  step size, and the linear position is tracked using MR compatible linear optical encoders (LIA 20-C001 30Z/9M, MV 61 - 10BP 00060, Numerik Jena, Jena, Germany) at a resolution of  $5\mu\text{m}$ . Similar to the rotary stepper motors, the linear stepper motors have a 7N holding force while unpowered. The Z-stage utilizes a feature where a triangular wedge forced to slide under a second triangular wedge that is constrained in all directions but the Z-axis. This  $30^\circ$  wedge feature was integrated into the Z-stage design to reduce the force required by the motors to lift the components by about 42% (assuming no effects of friction), which made it possible for the Z-stage to lift the

top wedge, Y- and X-stages, and the mouse bed using the combined force of two linear piezoelectric stepper motors. Due to the spatial constraints of the 9.4T MR scanner's 120mm diameter bore, the Z-stage was placed on the bottom with the Y-stage on top of it, positioning the Y-stage at the bore's widest point (see Fig. 5). The Y- and Z- stage DoFs were maximized since this robot has potential for other applications which require a larger range of motion.

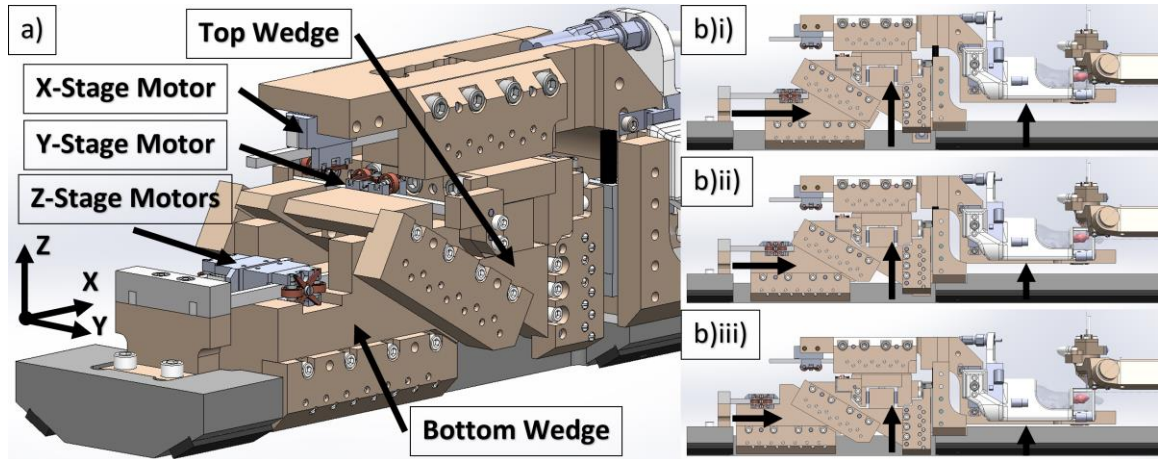


FIG. 5. A CAD model of the mouse bed attached to the XYZ-stage (a) illustrating the three controlled DoFs and (b) the Z-component of the mouse bed's wedge shim, depicting how it lifts the mouse bed (b)i-iii.

Due to the confined space in the MR scanner bore, the mouse bed could not be mounted on the top of the XYZ-stage; therefore, a cantilevered mouse bed was designed to hold the mouse's brain at the magnet's isocenter, underneath the RCM linkage (Fig 5(b)). Finite Element Analysis (FEA) provided an estimate of the deflection of the cantilevered mouse bed from the force of the needle insertion. The analysis incorporates a vertically applied force to simulate the highest vertical load on the mouse bed. The force value of 3 mN used in the FEA is representative of a 200  $\mu\text{m}$  flat punch probe insertion into the olfactory bulb,<sup>74</sup> resulting in an estimated maximum displacement of  $\sim 0.3$  micron (see Appendix 1 for the FEA results). The force estimate used in the FEA in the worst case scenario is expected to be much larger than the force required by the glass needles to penetrate mouse brain tissue in this study since the glass needles have a conical needle tip shape with a 10  $\mu\text{m}$  tip. Therefore, the cantilever mouse bed deflection due to the load applied during needle insertion is expected to be negligible.

Before being placed in the MR scanner for a brain scan, live mice are usually fixed into position and anesthetized using a bite bar to pull the snout into the end of the anesthetic delivery tube, while the body is taped to the mouse bed. Due to long scan times, live mice require a constant supply of anesthetic gas. The version of the mouse bed used in this study is not equipped with a bite bar or drug delivery tube, but the design allows space for these features to be included for *in vivo* experiments. Our 9.4T MR scanner is not equipped with a mouse bed, therefore the robot is pushed into the bore to a known length, which places the RCM close to the isocenter, and the mouse bed manipulator can then move the mouse brain to the isocenter.

## 2.4 Mechatronic System Design

Our needle delivery robot is controlled using a custom made controller, which is composed of four PIC® microprocessors (DSPIC33FJ128MC802-I/SO, Microchip, Chandler, AZ) arranged in a master/slave configuration. The Numerik Jena optical encoders output a differential sine-cosine signal that is subtracted through a differential amplifier (MAX492, Maxim Integrated, San Jose, CA) and then sent to the slave microprocessor that corresponds with one of that encoder's DoFs. The encoder's differential signal is designed to eliminate signal noise picked up by the encoder wires. The slave microprocessors control the motor positions based on the interpretation of the encoder's position feedback. The encoding information is relayed to the master microprocessor, which communicates with the computer. The desired orientation of the needle and position of the mouse bed manipulator are input into the control software module (written in MATLAB), which then uses a serial peripheral interface bus to communicate the desired position of each DoF to the controller's master microprocessor. Each slave microprocessor control switches on their respective motor drivers (PMCM21 Hand-held driver, PiezoMotor, Uppsala, Sweden) to control the motors. The controller system is constantly monitoring the position of each DoF and the motors activate at any time in order to reposition the motors to the set position, hence ensuring consistent positional accuracy.

## 2.5 9.4T MR Scanner

Our robotic device was designed for use in our Agilent 9.4T MRI system (9.4-Tesla 31cm bore Agilent animal MR imager with 120cm inner diameter 400mT/m gradient insert, Agilent, Santa Clara, United States of America) for small animals. The MR scanner's 120mm gradient coil bore-hole diameter is spatially limiting for robotic access, with the isocenter at ~90cm from the entry of the bore, hence increasing the complexity of the robotic design. The scanner can acquire 3D images with a spatial resolution down to 75  $\mu\text{m}$ , however, scanning at such a high resolution takes hours to complete. High resolution scans are difficult to perform on live mice since respiratory motion can cause the fixed mouse head to move up to 30  $\mu\text{m}$ . Since this is a research scanner, there is no built in body receiver coil, hence a custom surface coil is required, which inevitably reduces the amount of needle trajectories.

### 2.5.1 Radio Frequency Receiver Coil

A two-channel radiofrequency (RF) surface head coil was custom designed and fitted to the mouse bed (see Fig 6(a)). The thicknesses of the RF coil supports are minimized in order to maximize the clearance for the needle. The RF coil frame was 3D printed using fused deposition modeling (FDM) of polycarbonate; this material is commonly used in prototype RF coils since it has negligible MR signal, and hence no effects on the quality of the MR image. An MR visible cross-shaped fiducial embedded in the end of the mouse bed, directly under the mouse's head (see Figure 6(b)), is used to register the robot coordinates to the MR coordinates.

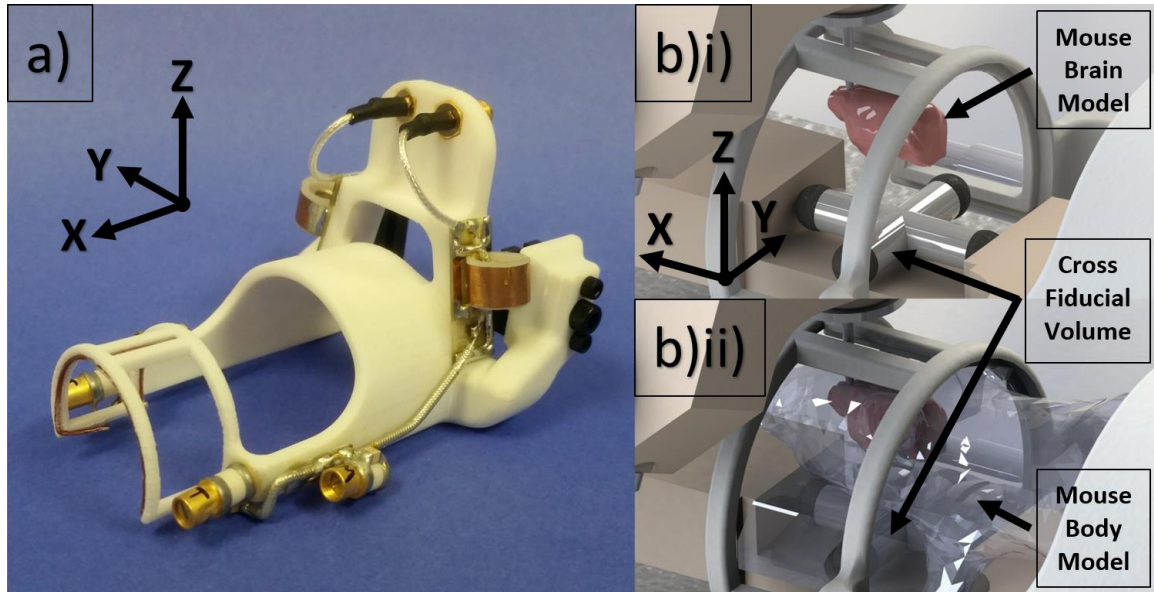


FIG. 6. (a) A picture of the two-channel surface RF coil. The RF coil frame was 3D printed using fused deposition modeling (FDM) of polycarbonate. (b) A Solidworks model render of the mouse bed and coil, with cross-fiducial water volume and mouse brain's approximate position (i) without the cross-fiducial Delrin housing or mouse body model, and ii) with a transparent cross-fiducial Delrin plastic housing and mouse body model.

## 2.6 Robot to MR Registration

The term “robot to MR registration” refers to the process of determining the position of the robot relative to the MR coordinates. A commonly used registration method employs the use of MR visible materials arranged in specific geometries that are clearly identifiable in the MR images. Through image processing and geometric calculations, the position of the fiducial can be determined in the MR images, as well as the position of other robotic components, such as the RCM.

### 2.6.1 Cross-Fiducial Design

Our registration approach incorporates a “cross” shaped fiducial<sup>55</sup> (from now on referred to as cross-fiducial), which has a simple, low profile, design that allows it to be easily embedded in the mouse bed, underneath where the mouse’s head rests (see Fig. 6(b)i). The cross-fiducial consists of two 4.38mm diameter perpendicular intersecting holes drilled through a piece of Delrin plastic, forming the shape of a cross. The holes are filled with water to provide contrast in the MR



images. The RF coil was designed to cover the mouse's head and the cross-fiducial in order to acquire a strong enough signal from the fiducial to be able to easily localize the fiducial in the MR images, and to calculate the position of the fiducial in the MR scanner's coordinate system. Magnetic field inhomogeneities are mainly the result of static magnetic field imperfections and magnetic field imperfections induced by the introduction of materials into the FoV, such as a robotic device. Through imaging techniques of the fiducial at specific orientations inside the MR scanner's bore, this localization fiducial design is insensitive to the effects of magnetic field inhomogeneity.

## 2.6.2 MR to Robot Registration Process

Acquiring 2D axial and sagittal proton density gradient echo images of the cross-fiducial oriented approximately perpendicular to the imaging planes results in images displaying a bright circle, where the center of the circle represents a point along one of the cross-fiducial cylinder's axes (TR = 5.76 ms, TE = 2.79 ms, flip angle = 11°, FoV = 32.00 × 32.00 mm<sup>2</sup>, matrix, size = 160 × 160, 51 slices, 0.50 mm slice thickness, 12 averages, acquisition time = 9:24 min). A fiducial cylinder's axis can be determined by locating the centroids of two circles in parallel MR images. Ideally, these images are as far apart as possible, on either side of the cross-fiducial intersection, in order to minimize the effect of the centroid localization error on the fiducial axis trajectory. Since the axes are unlikely to intersect, the closest point between the two axes becomes the location of the coordinate system origin. The two axes of the robot coordinate system are likely not perfectly perpendicular either, therefore, to extract a 3D Cartesian coordinate system from the two axes, the cross product of the fiducial axis perpendicular to the bore length and the fiducial axis parallel to the bore length yields the robot's Z-axis, the cross product of the fiducial axis parallel to the bore length and the Z-axis yields the Y-axis, and the Z-axis crossed with Y-axis yields the X-axis.

A semi-automated registration method developed in MATLAB uses pixel intensity masking to remove signal intensity variations from the fiducial, and locates the centroid of a circle

with a known radius of 4.38mm (~22 pixels in diameter using image parameters described above) using a built in circular Hough transform function<sup>75</sup>.

MR scanners shim the magnetic field to compensate for inhomogeneities, however magnetic field inhomogeneities can be caused by the introduction of foreign MR compatible material into the homogenous magnetic field. A method of compensating for in-plane magnetic field inhomogeneities is applied to the position localization of the cross-fiducial. By acquiring two of the same cross-sectional image sets of the fiducial with all things being equal, using the same pulse sequence with the frequency encoding directions reversed, the resultant average position of the fiducial in the frequency encoding direction corresponds to the true fiducial position in the MR scanner.<sup>76</sup> A benefit to the design of the cross-fiducial is that the cylinder axes of the cross-fiducials are in line with the MR coordinate system, hence slice select error caused by magnetic field inhomogeneities in registration images is also be negligible.

Using this method, a complete registration acquisition requires four image sets of the cross-fiducial: a set of 2D axial and sagittal images, and a second set with only the frequency encoding direction changed. Once the first image set is acquired, it is sent to the MATLAB folder where it can then be processed using the semi-automatic registration procedure while the next MR image set is being acquired, which takes less than 10 minutes per image set. Therefore, the entire registration procedure takes approximately 40 minutes. 2D image sets were chosen over a 3D image for speed, and to enable the fiducial localization correction. The MR images used to locate the fiducial had a large matrix size, so a much smaller matrix that is a few pixels larger than the fiducial cross-section would considerably reduce the registration time. The registration must be performed every time the robot is placed inside the MR scanner.

# Chapter 3

## 3 Experimental Methods and Results in the Development of an Ultra-High Field Strength MR Image-Guided Robotic Needle Delivery Device for In-Bore Small Animal Interventions

### 3.1 Experimental Methods

Methods were established to test the MR compatibility and mechanical accuracy of the robotic device as well as validate the device's needle targeting and trajectory accuracy.

#### 3.1.1 Effects of the Robot on MR Images

The introduction of any materials into the MR bore will have an effect on the magnetic field; some more than others. The distortion of the magnetic field, and consequently the images, is most prominent when a small amount of metal, including non-ferromagnetic metal, is present in, or near, the FoV. Electronics, such as motors and encoders, also emit RF signals, which can be obtained by the receiver coil and represented as noise in the MR images. The effects induced by the presence of a robotic device inside the MR scanner's bore are important to quantify in order to reduce their negative effects on the image quality.

### 3.1.1.1 Robot Induced Magnetic Field Distortion

The MR compatible Piezo LEGS Linear 6N piezoelectric motors selected to actuate the robot are made from non-ferromagnetic metals (primarily aluminum), therefore it is important to quantify the effects of the motors on the homogeneity of the MR scanner's magnetic field. The linear motor was used to distort the magnetic field instead of the rotary motor since some of the linear motors on the XYZ-stage were much closer to the imaging FoV than the rotary motors used to position the spherical linkage arms. The linear motors also contain more metal by weight than any other component on the XYZ-stage, and should induce the most distortion.

An accurately machined grid phantom was used to evaluate the distortions of the magnetic field, which is easier to visualize in the cross-sectional images of a grid phantom. The phantom was filled with water for high contrast between the Delrin geometries and the water filled voids. Coronal images were acquired of the phantom alone in the scanner, and the phantom with the motor placed in front of the phantom, to determine the amount of in-plane distortion caused by the motors. This experiment should determine the minimum distance that the robot's motors should be placed away from the FoV as to not distort the images. Gradient echo images were acquired of the phantom at a bandwidth of 20kHz and 50kHz, which are the low receiver bandwidth frequencies used when imaging mice. Lower bandwidths were used during gradient echo imaging in this experiment since more distortion occurs at lower bandwidth.

Coronal gradient echo images acquired without the motor present were subtracted from those with the motor present in order to visualize and observe the amount of distortion caused by the motors. The maximum observed in-plane distortion in the coronal images was at approximately 22.5mm into the phantom, from the closest side of the motor. Therefore, using a safety factor of 2, the location of the motors in the robot's design were required to be at least 45mm away from the edge of the closest FoV. Based on the amount of distortion caused by the linear motors, the comparative metal content between the linear and rotary motors, and the shortest distance between

a rotary motor and the nearest potential FoV (~250mm), the rotary motors should have no noticeable effect on the MR image quality (Note: the FoV can change depending on the position of the mouse bed manipulator).

### 3.1.1.2 Effect of the Robot on the Noise

The motors and encoders run at a maximum frequency of 2kHz and 5kHz respectively, while the MR scanner's RF receiver system operates at a center frequency of 400.2 MHz, hence the robot electronics should not have an effect on the image quality. The effects of the robot electronics on the MR images was evaluated through a RF spectrum scan performed to determine the signals present in the MR scanner's bore. The spectrum scan was performed with and without the robot in the 9.4T MR scanner's bore. Spectrum scans show a few noise signals between -165kHz and -185kHz from the center frequency while the robot was present and powered in the 9.4T MR scanner, which were not present when the robot was not present. Since the noise frequency is so far away from the center frequency of this scanner, the noise will only affect the image quality of echo planar imaging sequences which use a high receiver bandwidth (around 500kHz). The source of the noise is unknown.

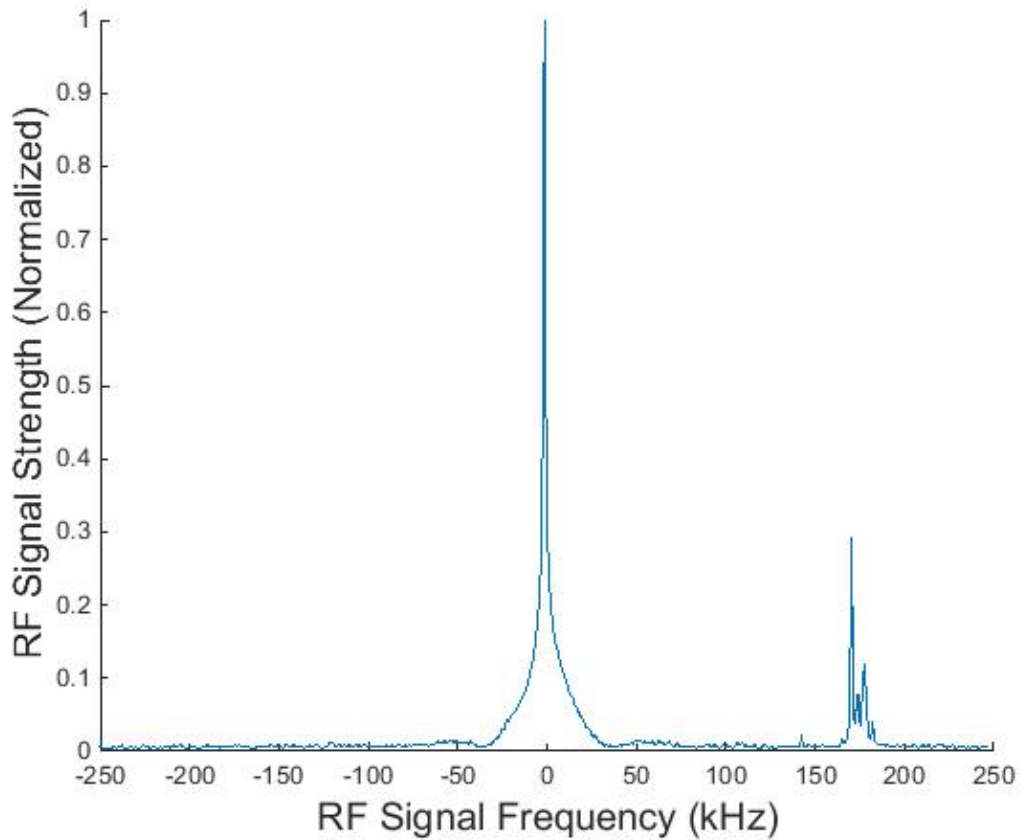


FIG. 7. Spectrum scan of RF signals present in the 9.4T scanner's FoV with the robot inside the MR scanner and present. A few noise signal peaks can be observed between 165kHz and 185kHz from the center frequency of 400.2MHz, which corresponds to 0 on the X-axis.

### 3.1.2 Calibration and Accuracy Experiments

A complete quantification of the robot's mechanical error was determined by measuring the individual error contributions of the mouse bed manipulator and needle manipulator linkage using a coordinate measuring machine (CMM). An improved needle length was calibrated based on the CMM measurements to reduce needle targeting error of the spherical linkage while the RCM to cross-fiducial registration calibration was performed in the 9.4T MR scanner.

#### 3.1.2.1 Open-Air Robotic Calibration and Accuracy Validation

The CMM (Global Image, Brown & Sharpe, North Kingstown, RI) was used to measure the position of the needle and the mouse bed manipulator to determine the open-air accuracy of the

robot, at a volumetric measuring performance (accuracy) of  $8.7\mu\text{m}$  with a repeatability of  $2.9\mu\text{m}$ . The needle delivery robot was retrofitted with tooling balls (Fig. 8) to act as features of known size and geometric accuracy on the robot's mouse bed manipulator and needle manipulator linkage for the CMM to measure. The positions of the spherical linkage tooling balls were measured at multiple needle trajectories, equally distributed along its range of motion. The vertical position of the needle was calibrated incrementally by trial and error using the CMM to determine the closest needle angle to vertical ( $0.048^\circ$  from vertical). To determine the needle trajectory and RCM, both tooling balls were measured in 24 orientations; at  $0^\circ$ ,  $22.5^\circ$  and  $45^\circ$  from the calibrated vertical position, at eight  $45^\circ$  increments around the vertical needle position (Fig. 3(c) illustrates the max angles measured by the CMM).

The mouse bed manipulator's orientation was measured at various positions throughout its working volume. The orientations were measured in a grid pattern at increments of  $6.25\text{mm}$  throughout X-Y-plane's  $25.40 \times 25.40\text{mm}^2$  RoM, and in five equally spaced horizontal planes, ranging from  $-6.25\text{mm}$  to  $6.25\text{mm}$  along the Z-axis. Twenty-five equally spaced measurements resembling a grid were performed in the home plane (X-Y plane when  $Z = 0$ ), while five position measurements were conducted for each of the other four X-Y-planes, only covering the center and four furthest corners of the planes. The position measurement of the center and four furthest corners of all five planes were re-measured to determine repeatability.

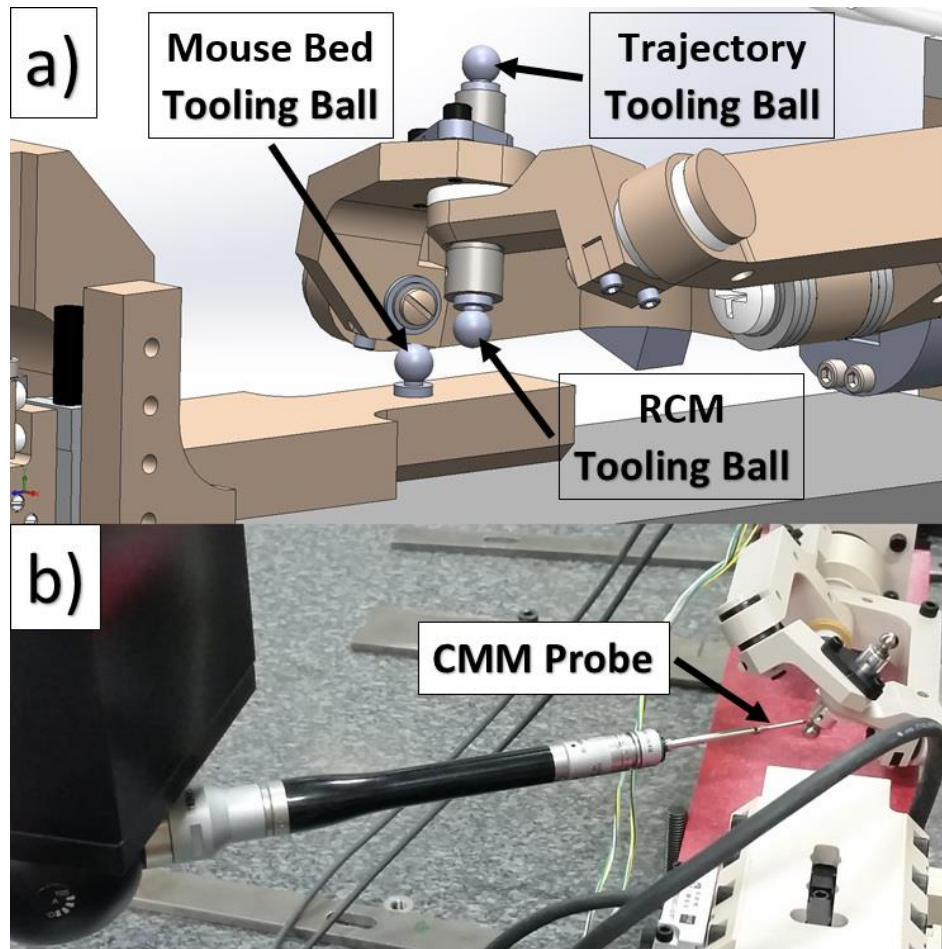


FIG. 8. (a) A CAD model of the robot retrofitted with tooling balls; one on the mouse bed manipulator, and two on the spherical linkage; one at the expected RCM and another along the needle trajectory. (b) The CMM probe touches five points on the tooling ball to determine the location of its centroid.

This measurement process also served as a calibration procedure since the actual tooling ball position is likely to differ from the CAD model positions due to additive machining and assembly errors. The linear rail bearings were designed with some clearance so the user could sense when the preload was being applied, and the relative amount of preload being applied to the bearings. Thus, as the pre-loading set screws are tightened, the outer set of rails of the linear rail bearing assembly are forced in the opposite direction of the set screw, resulting in a slight offset in the X-, Y- and Z-directions of up to 1mm (additive machining tolerances also contribute to this value). A similar pre-load induced offset is also present in the RCM linkage assembly due to the pre-loaded angular contact bearings that align the concentric arm controlling shafts and allow the shafts to rotate relative to one-another, however, in this case, the spherical linkage, including the



RCM, are shifted away from the mouse bed manipulator, along the axis of the concentric arm controlling shafts.

### 3.1.2.2 Hydraulic Needle Driver Needle Length Calibration

Due to additive machining errors, the designed RCM position and the RCM positions measured by the CMM differ. In reality, the RCM is within a spherical probability volume as opposed to a point. The length of the protruding needle from the extended hydraulic piston was designed to coincide with the RCM, however, this was not the case when the tooling ball representing the needle tip position was verified by the CMM measurements. The length of the needle protruding from the needle driver was adjusted in order to determine the needle length that produced the smallest needle tip error. This improved needle tip length was incorporated into the design of a jig, which was used to calibrate the needle length extending from the needle driver. In order to calibrate the needle tip position, the needle driver is inserted into the jig and screwed into place, then the glass needle is inserted into the piston while retracted (see Fig. 2(a)) and pushed a few millimeters past the expected clamping position. The piston is then extended, advancing the piston until the needle tip reached the bottom of the jig, at which point the piston continues to advance to the hard-stop, at which point the needle clamp is tightened to fix the needle in the piston at the improved RCM length.

### 3.1.2.3 Image Validation of Needle Accuracy in Phantoms

Due to minor design changes and repairs to the mouse bed manipulator after the CMM calibration, the robot required recalibration to confirm the relative position of the RCM and the cross-fiducial at the mouse bed manipulator's home position. The robot was placed in the MR scanner and the water filled glass needle was used to target preplanned virtual targets in a PVA (polyvinyl alcohol) phantom;<sup>77</sup> 10% PVA by weight and 90% water by weight, 1 freeze/thaw cycle. Seven different target and trajectory positions throughout the robot's working volume were imaged to calculate the position of the RCM relative to the cross-fiducial.

Image localization of the needle tip is not an accurate method of determining its location, since the needle tip diameter at the tip is about 10 $\mu$ m. The glass needles used in these studies are made using a pulled glass technique, meaning that the shape of the conical needle tip is not consistent among production batches. Therefore, a geometric registration of the needle tip is not a viable localization method. Instead, coronal image sets are used to locate two points on the axis of the water filled needle, which appear as bright spots in the MR images. The points along the needle trajectory axis are localized by determining the intensity-weighted centroid of the water inside the glass needle

$$x_C = \frac{\sum_i I_i x_i}{\sum_i I_i}, y_C = \frac{\sum_j I_j y_j}{\sum_j I_j} \quad (7)$$

where  $x_i$  and  $y_j$  are the pixel coordinates in the  $i^{\text{th}}$  row and  $j^{\text{th}}$  column,  $I$  is the pixel intensity, and  $x_C$  and  $y_C$  are the coordinates of the center of signal intensity in the image. The intensity-weighted centroid measurement approach was used instead of the MATLAB function used for fiducial localization because the needle trajectory is not perpendicular to the imaging plane, resulting in a more oval shape in the images. This method would be prone to localization error since the circular Hough transform function is designed to find circular shapes in images.

These scans were performed similarly to the scans used for the registration process previously described in Section 2.6.2, with the addition of coronal image sets, which were also re-acquired with reversed frequency encoding directions. Each image set in our study was imaged with six averages in a FoV of 32.00 $\times$ 32.00mm $\times$ 25.50mm<sup>3</sup>, with a voxel size of 0.200 $\times$ 0.200 $\times$ 0.500mm<sup>3</sup>. The average position in the two coronal image sets along the reversed frequency encoding directions were used to determine the points on the needle axis, insensitive to in-plane magnetic field inhomogeneity. Apart from the vertical needle orientation, the rest of the need axis orientations are not perpendicular to the coronal plane, hence there is no correction for slice select error.

The fiducial axis points and needle axis points were transformed into the global MR coordinate system using the output transform matrix from the MR scanner system. The needle axis points were transformed to the robot coordinate system derived from the fiducial axes. An iterative approach was performed to determine the point with the smallest average distance from the needle trajectories, at a resolution of 1  $\mu\text{m}$ . In other words, the RCM location that minimizes targeting error was determined. The location of the new RCM was found to be at -0.693 mm, -10.742 mm, -0.001 mm in the X-, Y- and Z-directions, respectively, in the robot coordinate system.

### 3.1.3 Total Image-Guided Needle Accuracy Validation in Phantom Tissue

The complete needle targeting and insertion procedure was performed identically to the one described in Section 3.1.2.3 but with nine different targets and needle orientations, covering the robot's working volume for mouse brain procedures. The robot was removed from the bore and re-inserted after each needle orientation, to ensure that the fiducial was not in the exact same position or orientation inside the MR scanner's bore during the robot registration. The shortest distance from each needle axis to the newly calibrated RCM, determined in Section 3.1.2.3, was computed to determine the total needle targeting and needle angle errors of the needle delivery procedure.

### 3.1.4 *In Situ* Needle Delivery Accuracy Validation

A medium sized mouse (~35g) was obtained and used as an *in situ* test subject to validate the needle targeting procedure in a small animal. The mouse was ethically euthanized according to institutional procedures and a craniotomy was performed to provide access to the brain. The glass needle was filled with water to create a large contrast between the needle and brain tissue to ensure that the needle can be visualized in the post-insertion images. The spherical linkage and mouse bed manipulator were moved to positions, which allowed the user enough room to load the mouse and RF coil onto the mouse bed. Double-sided tape was placed on the mouse bed while tape was placed

around the body and snout to help fixate the mouse. The mouse's head was oriented so that the area of exposed brain was not covered by the RF coil (see Fig. 9). The robot was placed in the MR scanner's bore and advanced until the mouse's brain was at the MR scanner's isocenter. The registration procedure was conducted as described in Section 3.1.2.3. The third dorsal ventricle was selected as the needle target for this experiment since a mouse's ventricles have high contrast in MR images and intraventricular injections are commonly performed in small animals<sup>78</sup>.

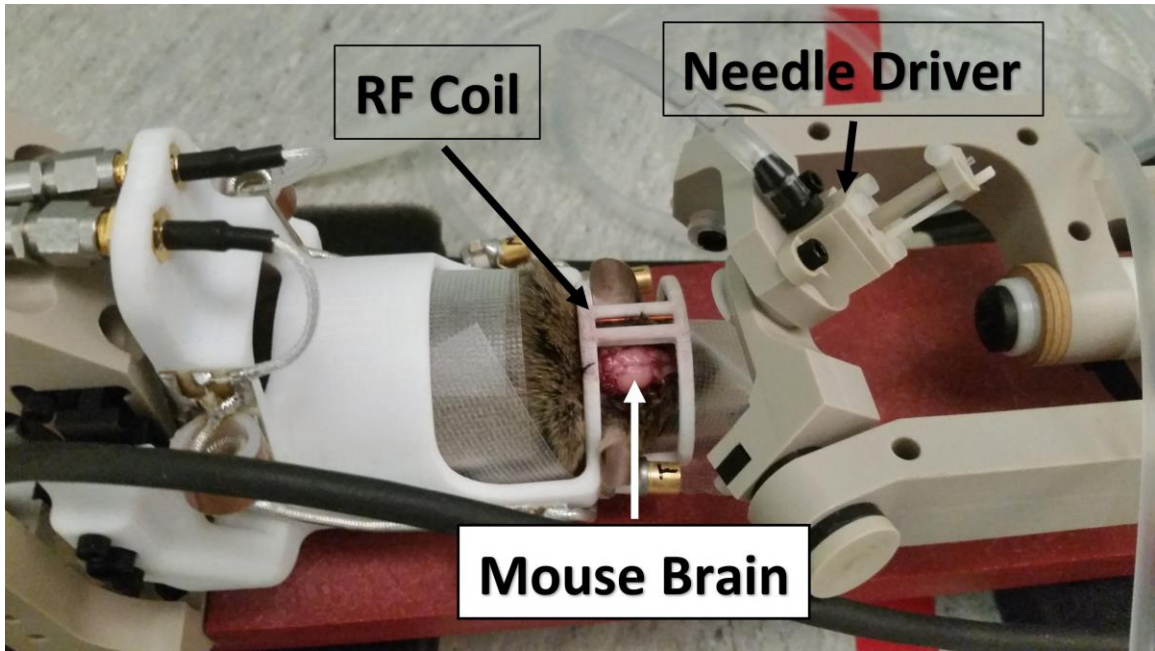


FIG. 9. Picture of the robotic device with the mouse taped to the mouse bed with the RF coil placed over top of it. The X-stage is moved as far backwards as possible and the spherical linkage is moved away from the mouse bed to provide access to the mouse bed during setup.

A target point was selected in the mouse's ventricle and a second point was selected to define the needle's trajectory in the MR images. The same voxels were also selected in the images with reversed frequency encoding directions. The target and trajectory coordinates were processed to determine the target position and needle trajectory relative to the robot, and subsequently, the encoder coordinates for the five DoFs. Once the robot was moved to the targeting position, a 3D image was acquired of the brain (steady-state free precession, TR = 7.00ms, TE = 3.50ms, flip angle = 30°, FoV = 19.20 × 19.20 × 19.20mm<sup>3</sup>, matrix size = 128 × 128 × 128, 150μm isotropic, 4 averages, 4 frequencies, acquisition time = 30:35 min). The needle driver was manually actuated,

plunging the glass needle tip through the mouse brain and into the ventricle. 3D images of the mouse brain were also acquired with the glass needle in the brain and when the glass needle was removed from the brain.

## 3.2 Results

The results from the accuracy validation experiments are displayed in Table 1 and are discussed in the following subsections.

Table 1: Summary of all positional and angular error results from the various accuracy validation experiments outlined in Section 3.1.

Experiment	Error	Measurement Method
<b>2.2.6.1 Open-Air Robotic Calibration and Accuracy Validation</b>		
Total Needle Tip Position Repeatability Error	$146 \pm 38 \mu\text{m}$	CMM
Needle Tip X Position	$24 \pm 28 \mu\text{m}$	CMM
Needle Tip Y Position	$32 \pm 16 \mu\text{m}$	CMM
Needle Tip Z Position	$140 \pm 21 \mu\text{m}$	CMM
Total Needle Trajectory Angle Repeatability Error	$0.15 \pm 0.62^\circ$	CMM
<b>2.2.7 Total Image-Guided Needle Accuracy Validation in Phantom Tissue</b>		
Total Robot Needle Targeting Error	$178 \pm 54 \mu\text{m}$	MRI
Total Robot Needle Trajectory Angle Error	$0.27 \pm 0.65^\circ$	MRI

### 3.2.1 Open-Air Calibration and Accuracy Testing

A CMM was used to iteratively calibrate the vertical needle position to an angle of  $0.048^\circ$  to the vertical. This position was assumed to be the vertical position of the needle in the kinematic equations, and hence the rest of the needle trajectories were based on the initial trajectory. The mean positional error of the RCM tooling ball was measured to be  $83 \pm 47 \mu\text{m}$ , with a mean trajectory angle error of  $0.15 \pm 0.62^\circ$  throughout the 24 measured orientations. The length of the needle was virtually shortened and lengthened iteratively in the CMM data set until the standard deviation was minimized. The needle length required a  $76 \mu\text{m}$  extension from its current length

based on the CMM results, which reduced the mean positional accuracy of the spherical linkage to  $146 \pm 38 \mu\text{m}$ . Although this extension increased the mean needle error, it reduces the standard deviation which will result in more consistent needle targeting. The true location of the RCM with the extended needle tip was used as the calibrated RCM for future procedures. The new needle tip position information was used in designing the needle length calibration jig described in Section 3.1.2.2.

The calibrated home position of the mouse bed manipulator was determined and was measured at 45 different positions over its RoM, however, the mouse bed manipulator's entire working volume is much larger than what is needed for mouse brain experiments,  $25.4 \times 25.4 \times 12.5 \text{mm}^3$  and  $\sim 10 \times 15 \times 10 \text{mm}^3$  respectively, and therefore a working volume of  $12.5 \times 12.5 \times 12.5 \text{mm}^3$  is a more accurately representative of the mouse bed manipulator's error for brain procedures. This cubic mouse brain working volume was used because the calibration positions were measured in increments of 6.25mm or less in all three directions. Therefore, the mean positioning error of the mouse bed manipulator throughout the working volume of the mouse brain is  $31 \pm 58 \mu\text{m}$ .

### 3.2.2 Needle Tip Accuracy in Phantom Tissue

The image-guided needle targeting accuracy was determined in PVA phantom tissue. The water filled needle was inserted into the phantom at nine different targets and trajectories. Each needle trajectory was imaged to determine the trajectory of the needle from the image (see Fig. 10). The mean needle targeting accuracy in an MR image-guided phantom procedure was  $178 \pm 54 \mu\text{m}$  with a mean trajectory angle error of  $0.27 \pm 0.65^\circ$ .

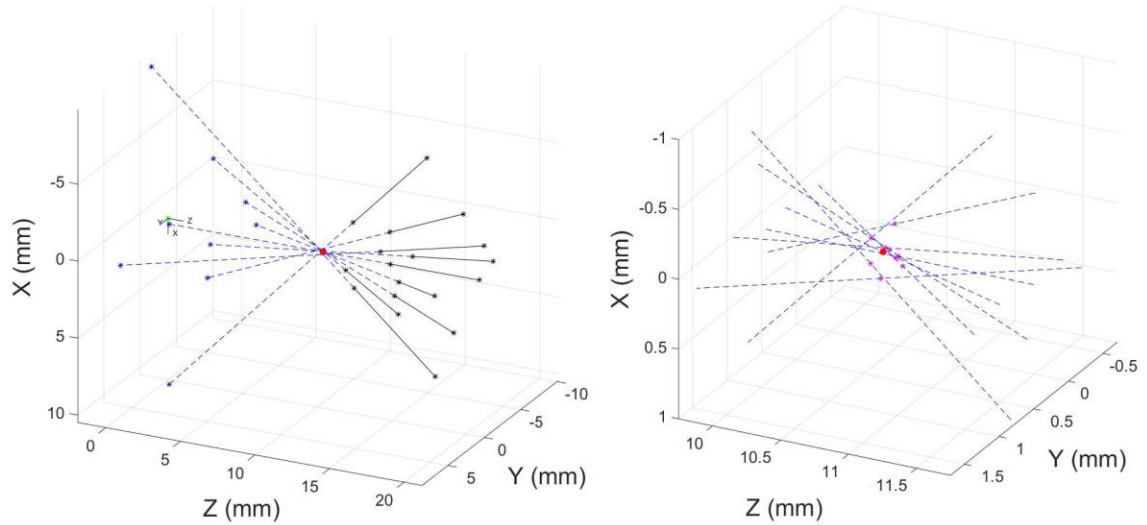


FIG 10: Plot of the needle trajectories from the image-guided phantom targeting experiment. The graph on the right is zoomed in to illustrate the distance between the RCM and the needle trajectories. A 2D image set was acquired of the needle protruding from the phantom tissue at each of the nine needle trajectories. Two points on the needle axis were localized in the MR images and their positions transformed into robot coordinates. Since the mouse bed manipulator moves to align the target in the mouse brain with the fixed RCM, the relative needle trajectories are offset by the distance the mouse bed manipulator has had to move in 3D for each needle orientation. These mouse bed manipulator's encoder position were subtracted from the needle trajectory points in order to align the trajectories relative to the RCM. These trajectories were used to calculate the shortest distance from each trajectory to the RCM. Each needle trajectory is represented by black asterisks connected by a solid black line, where the black asterisks are the points along the needle axis localized in the MR images. The red dot at the junction of the needle trajectories is the location of the calibrated RCM, while the magenta asterisks, seen more clearly in the graph on the right, represent the closest point on each trajectory to the calibrated RCM.

### 3.2.3 In Situ Preclinical Application

A preclinical image-guided needle targeting demonstration was performed in the third dorsal ventricle of a mouse brain. The target inside the third dorsal along with the needle trajectory point was selected from 2D MR images acquired during the registration procedure. 3D images were acquired after the needle insertion and after the needle was removed (see Fig. 11).

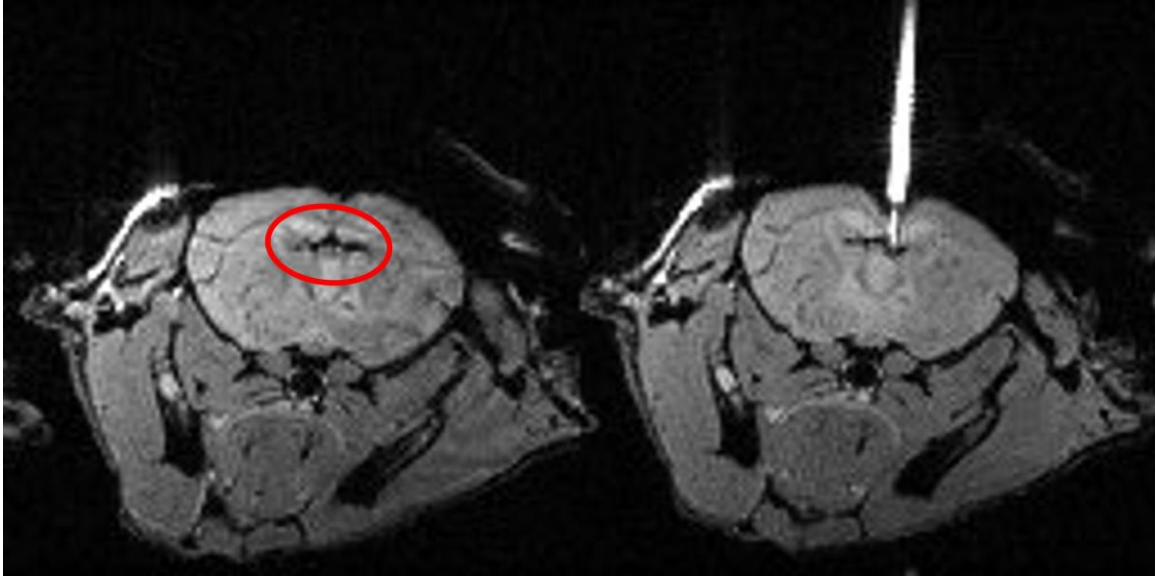


FIG. 11. Axial slices from the 3D mouse brain images, a) before needle insertion with red oval around the black ventricle, b) with the needle inserted in the lateral part of the third dorsal ventricle.

## 3.3 Discussion

### 3.3.1 Effects of the Robot on MR Images

Any negative effects of the robot on the MR images are likely detrimental to the success of this robot since the accuracy of registration and needle target/trajectory selection are directly related to the accuracy and quality of the MR images.

The magnetic field distortion experiment indicated the approximate measurement of in-plane distortion caused by the metal linear MR compatible piezoelectric motors. The incorporation of this design constraint ensured that the accuracy of the robot localization was not compromised by distorted images, which was key to the overall success of the robot.

The fundamental principle of MR imaging is based on receiving RF signals from the imaging samples. Noise can easily be introduced into the MR scanner by foreign electrical components such as motors and encoders. The spectrum scan showed a few small unknown noise signal peaks between -165kHz and -185kHz from the center frequency (400.2MHz). These unknown signal peaks would likely introduce error into MR images acquired at a BW higher than



330kHz, such as echo planar imaging, which use high bandwidths around 500kHz in the 9.4T scanner. The noise signals will not affect the images acquired using any lower bandwidth scanning sequences. Although most gradient echo sequences use a much lower bandwidth than 330kHz, there are some that use higher bandwidths, which will be more susceptible to noise artifacts.

The effects of the magnetic field inhomogeneity on fiducial localization were calculated by comparing the locations of the fiducial localization points in the first image sets with those from the second image set with reversed frequency encoding directions. Based on the registration images acquired for the robot registration during the phantom tissue experiment, the mean difference between the localized fiducial positions in the images with the initial and the reversed frequency encoding directions was  $2 \pm 61\mu\text{m}$  and  $13 \pm 54\mu\text{m}$  in the axial and sagittal planes, respectively. Since the mean difference in position localization is relatively small, the effects of magnetic field inhomogeneity on the localization accuracy were deemed to be negligible. The large standard deviation can be attributed to the fiducial localization error. This calculation yielded negligible effects, indicating that the in-plane localization error induced by magnetic field inhomogeneities pose negligible effects. The 9.4T MR scanner, as with most modern MR scanners, employ shims, which correct the scanner's magnetic field inhomogeneities due to main magnetic field imperfections and due to the presence of foreign objects. The effects of magnetic field inhomogeneity are also reduced when imaging at a higher bandwidth. The 2D registration images were acquired at a bandwidth of 40kHz, which is above average.

### 3.3.2 Open-Air Calibration and Accuracy Testing

The in-air calibration and accuracy testing using a CMM proved to be a valuable step in the development of this robot, especially considering that the needle tip length adjustment enabled an increase in the RCM accuracy of over 20%.

The standard deviation of the needle trajectory error at 45° was about twice as large compared to the average trajectory error (see Table 2). This large standard deviation was unexpected considering the effective step resolution of each controlled spherical linkage arm was 0.09°. Similar to the trajectory error, the needle targeting error from the spherical linkage also increases substantially as the needle angle approaches 45°.

Table 2: Table demonstrates the increase in mean targeting and trajectory errors as the needle angle increases relative to the vertical position.

Needle Angle from Vertical	n	Mean Trajectory Angle Error	Deviation of RCM Position Error (μm)		
			X	Y	Z
0°	8	0.147 ± 0.061°	± 5	± 5	± 15
22.5°	8	0.085 ± 0.104°	± 19	± 18	± 16
45°	8	0.522 ± 0.995°	± 47	± 22	± 24

The causes of this error became more evident once the individual trajectory errors were analyzed. The spherical four bar linkage design used for this robot possesses a non-linear angular position relationship between the controlled arms and the needle. In other words, for each angular step of the controlled arms to the needle angle forward, the change in needle angle step size decreases, and the opposite occurs when the needle is angled backwards (see Table 3).

Table 3: Non-linear relationship between encoder step size and needle trajectory. These needle angles and encoder step sizes are representative of the needle trajectory confined to a vertical plane of the needle tilting forwards and backwards (Figs. 3(c)iv and 3(c)vi), respectively). The required encoder positions were calculated based on one degree planar movements of the needle trajectory.

Needle Angle	Controlled Spherical Linkage Arm Angle	Difference	Encoder Steps
45° backwards	81.33°	0.22°	2.44
44° backwards	81.11°		
0° (vertical)	68.66°	0.40°	4.39
1° forwards	68.26°		
44° forwards	30.97°	2.46°	27.33
45° forwards	28.51°		

As seen in Table 3, the needle's angular positioning resolution is over ten times higher when the needle is fully angled forwards compared to when it's angled backwards. The needle trajectories were calibrated relative to the vertical needle position, and is therefore it is expected

that the trajectory error increases as the needle travels away from the calibrated position. Also, as the needle is tilted backwards, the moment arm of the applied force from the controlled linkage arm to the passive linkage arm decreases, in turn requiring more force to move the linkage. Therefore, since more force is required to overcome the small moment arm, the added force on the joint between the controlled and passive arms results in more friction in the joint, making it more difficult to move the hydraulic needle driver at these angles. This added force is also the source of temporary deformation of the linkage, considering all of the parts, including fasteners, are plastic. A combination of these effects are most likely the cause of the increase error when the needle is tilted backwards. Although the trajectory error's standard deviation is higher than expected, the result is still within the target mean of  $<1^\circ$ . The scenarios where the effects of higher trajectory error would have an effect the procedure are regarding the ability of the system to drive the needles through a small burr hole, without the needle interfering with the skull or RF coil, and to avoid any sensitive areas of the brain. In a worst case, and almost unrealistic scenario for mouse brain injections, if the vertical target depth was 10mm, a needle trajectory of  $45^\circ$  would require the needle to pass through about 14.14mm of brain tissue. If a needle trajectory error of  $1^\circ$  was added to the desired needle trajectory, resulting in a  $46^\circ$  trajectory angle, the needle would enter the brain tissue about 0.35mm over from the expected entry point. The effects of the maximum potential error are important to consider during the procedure. However, since the mouse brain targets are usually relatively shallow, the effects of a mean trajectory angle error of  $<1^\circ$  should keep the needle trajectory within a safe distance from intersecting any sensitive/restricted areas of the brain.

Other sources of error in this measurement method include the slight deformation of the device due to the relatively small applied force of 0.07N on the components being measured, as well as the error of the CMM itself.

### 3.3.3 Needle Targeting Accuracy in Phantom Tissue

The needle targeting experiment in phantoms successfully yielded a calculated mean targeting accuracy of  $<200\mu\text{m}$  and a mean trajectory angle accuracy of  $<1^\circ$ . A limitation of the trajectory based needle targeting accuracy measurement method remains that the actual position of the needle tip was not measured, but rather the shortest distance between the RCM and the needle trajectory was assumed to be the error. Although this targeting accuracy measurement is not perfect, many measures have been implemented to validate the device's needle targeting accuracy, including the CMM calibration and accuracy measurements, the implementation of the needle length jig, and the RCM calibration with MR images. This needle targeting accuracy measurement method neglects the deformation of tissue, potentially resulting in the needle tip coming up short to the target. The effect of tissue motion on the needle targeting accuracy is expected to be relatively small in preclinical brain applications considering the extremely fine glass needle tip (which pierces tissue with ease), low density brain tissue, slow needle insertion speed, and the shallow brain targets. This needle targeting accuracy measurement method also neglects the effects of needle deflection, but since the needle tip is symmetrically pointed (conical), as opposed to a beveled needle tip, it is unlikely that an unbalanced lateral load will be applied to the needle upon insertion. The target depths are also only a few millimeters deep, so internal tissue forces are unlikely to deflect the needle to any meaningful degree. The needle will likely break if a foreign lateral force is applied to the needle, close to the needle's tip, since it is very thin ( $\sim 1\text{mm}$ ) and because glass has a low tensile strength. Based on the device's intended purpose in this application, it is unlikely that the needle deflection has any impact on the targeting error of this device.

Although the fiducial localization error and needle axis localization errors contribute to the overall measurement of the device's targeting error, the error patterns were consistent between the CMM and phantom needle targeting validation experiments. This indicates that these localization errors don't have an exaggerated bias in the device's accuracy measurements.

The long registration time can be a major disadvantage of using this device. In our *in situ* application, the needle target was relatively large, and therefore a voxel volume of  $0.2 \times 0.2 \times 0.5 \text{ mm}^3$  provided sufficient detail to distinguish the target. Since no meaningful in-plane magnetic field inhomogeneities were detected, the correction method requiring two acquisition of each image set is unnecessary. Therefore, the registration process only needs two image sets in total (as opposed to 4), hence reducing the registration time by half, to ~20 minutes. This registration time can then be further reduced to ~10 minutes by fitting the fiducial within a tight image matrix of  $40 \times 40$  pixels without changing the voxel size.

### 3.3.4 In Situ Preclinical Application

The device successfully demonstrated an ultra-high field strength MR image-guided in-bore needle targeting intervention where the tip of a glass needle was guided into the third dorsal ventricle in a mouse brain. Image confirmation shows the water filled needle penetrating the mouse brain and entering the ventricle (see Fig. 11(b)). As previously mentioned, the actual needle tip cannot be visualized since it is about  $1/15^{\text{th}}$  of the voxel's size. The ventricles in live mice are generally bright in the MR images, however, CSF is known to evacuate from the ventricles after a craniotomy in euthanized mice, resulting in much less signal from those areas.

## 3.4 Conclusion

The design, calibration and experimental accuracy testing of an MR image-guided robotic needle delivery device has been developed to successfully perform needle targeting procedures with a mean targeting error of  $<200 \mu\text{m}$  and a mean trajectory error of  $<1^\circ$ . The robot should provide researchers with a user friendly tool for conducting accurate and repeatable preclinical needle targeting procedures in soft tissues such as mouse brains. The six DoF robot was manufactured from MR compatible materials, predominantly plastics, and is controlled using MR compatible piezoelectric motors and optical encoders. The robotic design focused on minimizing the effects of

the robot on the image quality since the image registration process relies directly on the accuracy of the MR images. An MR visible fiducial was built into the robot's mouse bed to localize the robot's position and orientation in the MR images through a semi-automated registration procedure. The registration and kinematics are computed in MATLAB based on the needle target and trajectory selected in the MR images, which are transformed into the robot coordinate system from which the device can be positioned to conduct the needle insertion procedure. The device's mechanical calibration and accuracy measurements were conducted using a CMM, reporting a mean open-air needle targeting and trajectory error of  $146 \pm 38\mu\text{m}$  and  $0.15 \pm 0.62^\circ$  from the spherical linkage, respectively, and a mean mouse bed manipulator error of  $31 \pm 58\mu\text{m}$ . These mean position errors were used as the calibrated positions. An evaluation of the device's total targeting error was evaluated by performing needle insertions to nine different targets at various trajectories throughout the device's working volume. The accuracy of the device was measured using the relative position of needle trajectories to the RCM in the MR images, yielding a mean needle targeting error of  $178 \pm 54\mu\text{m}$  and a mean trajectory error of  $0.27 \pm 0.65^\circ$ . Finally, the device successfully demonstrated an image-guided needle targeting procedure *in situ*.

# Chapter 4

## 4 Summary and Future Work

### 4.1 Summary

#### 4.1.1 Chapter 2: The Design of an Ultra-High Field Strength MR Image-Guided Robotic Needle Delivery Device for In-Bore Small Animal Interventions

A six DoF robotic device was designed, developed and tested to perform needle interventions in small animals under ultra-high field strength MR image-guidance. Mechanical and electronic design constraints stemming from the nature of ultra-high field strength preclinical MR scanners resulted in the development of a unique, compact, robotic device, designed to work inside the MR scanner without degrading the quality of the images. The robot is composed of three main components: the needle driver, used to insert and retract the glass needle; the spherical linkage, used to manipulate the trajectory of the needle driver; and the three linear DoF mouse bed manipulator. The robot utilizes MR compatible piezoelectric motors to actuate five DoFs, while the needle driver is actuated using a miniaturized hydraulic design. The position of each DoF is tracked using MR compatible optical encoders.

An MR visible cross-fiducial structure was used to locate the robot inside the MR scanner's bore. The fiducial structure was integrated into the mouse bed, directly under where the mouse's head rests. This fiducial shape, in conjunction with specific imaging sequences, can eliminate the sensitivity of the fiducial localization error due to magnetic field inhomogeneity<sup>55</sup>. A MATLAB program was developed to identify the cross-fiducial in the MR images, which was subsequently

used to calculate the location of the desired target, selected from the MR images, relative to the robot.

The robot controller uses four PIC microprocessors, arranged in a master/slave configuration to process and communicate the encoder positions to the MATLAB program, where the desired encoder position is calculated and set based on the selected target and needle trajectory determined from the MR images. The motors actuate the robot until the desired position is reached, when the target coincides with the spherical linkage's RCM, at which point the needle can be inserted to the target.

#### 4.1.2 Chapter 3: Experimental Methods and Results in the Development of an Ultra-High Field Strength MR Image-Guided Robotic Needle Delivery Device for In-Bore Small Animal Interventions

A CMM was used to calibrate, and validate the open-air accuracy of the device by retrofitting the needle driver and mouse bed manipulator with tooling balls. The spherical linkage and mouse bed manipulator were moved to 24 and 45 positions, respectively, covering their RoM. After calibration, the spherical linkage's open-air needle targeting and trajectory errors were  $146 \pm 38\mu\text{m}$  and  $0.15 \pm 0.62^\circ$ , respectively, and a mouse bed manipulator had a mean positioning accuracy of  $31 \pm 58\mu\text{m}$ . These mean position errors were used as the calibrated positions.

A PVA phantom was molded and mounted to the mouse bed to simulate needle deliveries in mouse brain tissue. A total of nine needle insertions were performed with different targets and trajectories throughout the normal working volume of the device during brain targeting procedures. The glass needle was filled with water so it could be visible in the MR images, and therefore localized in the MR images to determine the device's accuracy. The mean targeting error of the



device was  $178 \pm 54\mu\text{m}$  with a trajectory angle error of  $0.27 \pm 0.65^\circ$ , which are within the objective mean errors.

An *in situ* needle targeting experiment was performed to demonstrate the capabilities of the system to select a target and trajectory from the MR images, and accurately deliver a needle to the target. In this case, the device performed a needle delivery to the third dorsal ventricle of the mouse brain.

## 4.2 Conclusion

The field of preclinical image-guided interventional robotic devices has seen continuous developments, fueled by the progress and advancements of medical imaging technology and preclinical models. Minimally invasive image-guided interventions boast a variety of benefits, including minimized trauma to the mouse as target exposure is unnecessary. An MR image-guided needle delivery robot combines the benefits of ultra-high field strength MR imaging's high spatial and contrast resolution, while the use of an MR compatible robot for needle manipulations can provide high resolution needle positioning to ensure safe and accurate injections. The development of this preclinical tool should also serve to simplify the overall preclinical injection process. A CMM was used to perform the robot's mechanical calibration and open-air accuracy evaluation to ensure the robot is sufficiently accurate. The robot was registered to the MR coordinates using an MR visible fiducial. An evaluation of the device's total targeting and trajectory errors was performed in phantom tissue, yielding a mean targeting error of  $<200\mu\text{m}$ , and a mean trajectory angle error of  $<1^\circ$ . Finally, an image-guided needle targeting procedure successfully demonstrated *in situ*.

## 4.3 Future Work

Although the proof-of-concept was successful, there are numerous refinements and developments that need to be implemented before this device can be used as a practical tool for a wide range of preclinical research techniques.

### 4.3.1 Mechanical Design Improvements

The spherical linkage and mouse bed manipulator both performed to within the expected standard of accuracy. As previously discussed, it is considerably more difficult to achieve the same targeting accuracies in plastic mechanical devices compared to those constructed from metal. The calibrations performed to the spherical linkage by iteratively adjusting the needle length to minimize needle targeting error and accurate positioning the needle vertically were important in reducing targeting and trajectory errors, respectively. The mouse bed manipulator's position was calibrated, but there was not attempt to map and correct the error contributions for each DoF. The mouse bed manipulator had a mean positional repeatability of  $\pm 15\mu\text{m}$  (25 positions measured twice each over the RoM of the mouse bed manipulator), indicating that the integration of a 3D map of the mouse bed manipulator's error into the positioning software would be able to improve the device's overall targeting accuracy.

The most challenging aspect of the robotic design was the integration of a non-metallic, bi-directional, needle driver. The current hydraulic design proved to have some functional issues, where it was occasionally unable to retract the needle, indicating that an alternate design solution may be required. The current needle driver design is a manually actuated using a syringe, which advances the needle when compressed, and retracts the needle using suction by pulling back the syringe. The hydraulic piston, which is coupled to the needle, contains an O-ring seal which prevents the hydraulic fluid from escaping from the hydraulic housing, especially while under higher pressures during actuation (see Fig. 2 for a cross-sectional view of the hydraulic needle

driver). The difficulty in this hydraulic design remains that the O-ring seals needs to be tight enough to keep the hydraulic fluid from escaping under pressure, but loose enough for the hydraulic piston/needle to be retracted by suction. Since the suction in this design is a much weaker pressure than hydraulic compression, the needle driver would occasionally be unable to retract the needle. To overcome the issue regarding actuation from suction pressure, commercial bi-directional hydraulic actuators are generally composed of two hydraulic cylinders acting in opposite directions, which allows the actuator to insert or retract the piston/needle using the same amount of controlled force. Designing a bi-directional hydraulic actuator for this application is difficult due to the lack of space. A potential solution involves replacing the hydraulic actuation with pneumatic actuation for the needle insertion, and a vacuum to apply suction and for needle retraction. While the maximum amount of suction produced by the syringe was limited by the stroke volume of the syringe, an external vacuum has the ability to apply an increasing amount of suction in order to overcome the friction within the needle driver. The pneumatic actuation could be provided through the same tubing currently used for hydraulic actuation, and allowing the pneumatic components be set up outside of the MR suite, therefore not requiring them to be MR compatible. This design solution would integrate well with the current robotic design, since the robot would not require a redesign.

Before performing needle targeting procedures in live mice, the bite-bar and anesthetic tube connector assembly must be manufactured, and alterations need to be made to the mouse bed so the bite-bar and anesthetic tube connector assembly can be integrated onto the mouse bed. The bite-bar and anesthetic tube connector assembly were incorporated in the original CAD design to insure that there was no interference between it and the spherical linkage throughout the device's RoM.

A suggested mechanical design improvement involves the integration of a needle depth control feature during needle insertions. This feature poses a design challenge since the linear

position encoding requires the use of an electrical encoder with high accuracy, which needs to be located on the needle driver, and therefore too close to the FoV. However, this approach would likely result in image artifacts. A potential solution to track the needle insertion depth involves the integration of a spherical MR visible fiducial that is mounted on the proximal end of the needle, where it exits the piston. The position of the needle fiducial relative to the RCM can be calculated to determine the needle insertion depth. The disadvantage of this method is that this image based position tracking is not as accurate as mechanical encoding. The imaging FoV would also need to be enlarged, or a separate scan may need to be performed, in order to visualize the needle fiducial depending on the depth of the insertion, therefore prolonging the overall needle targeting procedure.

The RF coil was designed to be placed over the mouse after the mouse was fixed to the mouse bed. A potential design improvement involves flipping the RF coil from its convex orientation to a concave orientation and integrating it directly into the mouse bed. This new arrangement boasts many benefits, including: improved user friendliness since the user would not need to place the RF coil over the mouse after fixation; improved registration time since the fiducial is closer to the RF coil, resulting in higher signal from the fiducial and therefore requiring fewer averages; and this orientation of the RF coil would not impede and needle trajectories.

Although this study focuses on brain injections, this device was designed with a detachable mouse bed to accommodate the use of custom mouse beds and RF coil designs tailored to other local targeting procedures anywhere within the mouse's body. Additionally, a wide variety of needle shaped tools can be placed in the hydraulic piston's cannula to perform a variety of procedures, including pressure measurements, biopsies, electrode placements, ablation, etc. This robot has created the potential for numerous high-accuracy preclinical targeting applications, which were previously difficult with unreliable accuracies.

## 4.3.2 Controller Improvements

### 4.3.2.1 Electronic Improvements

The electronic controller developed for this robot uses a mix of prototyped and stock electronics. The current design is made up of various components, which need to be individually connected before each procedure resulting in added time to the pre-procedure setup. The stock piezoelectric motor drivers were finicky and some of them often required resetting after the controller was all assembled and connected, which can only be done by unplugging and plugging in the power cable. The electronic components should be integrated into a control box for protection, and external switches should be added to make setup easier and faster. Other minor improvements include replacing the small/weak wire connectors on the motor cable extensions, and replace them with more durable and user friendly connectors.

### 4.3.2.2 Software Improvements

The current control and registration software are functional but could be improved with a proper user interface to allow the user to perform all of the necessary tasks in one user friendly display.

A vital software tool that needs to be implemented to improve the robot's usability involves the automatic detection of "no-go" zones, in which the software will not permit the user to position the robot in a way in which any part of the robot could collide with any other part of the robot. It is an important feature to ensure that the glass needle tip is protected since it is very fragile. If the needle tip were to break due to unintentional contact as the needle was being inserted, the procedure would have to be halted, the robot would need to be removed to replace the needle and injectable material, and the registration procedure would need to be performed again. The effect of breaking a glass needle may result in a glass shard coming in contact with the exposed area of the brain or skull. Alternatively, the risk of a collision between the needle tip and the RF coil can be eliminated by implementing the "flipped" RF coil design discussed in Section 4.3.1. Other "no-go" zone

applications should eventually include the auto-segmentation of sensitive regions of the brain, and of the burr hole, to ensure that the needle trajectory is automatically constrained to passing through the burr hole.

### 4.3.3 Registration Procedure

The chief improvement of the registration procedure involves creating a completely automated registration algorithm as opposed to the current semi-automated version currently being used. The registration and position control software should be integrated into MR scanner's control computer, allowing the software to instantly access the image files to perform the image registration, and eventually the "no-go" zone auto-segmentation.

A drawback of any medical robotic device is the need for it to be recalibrated if major components need to be taken apart and reassembled for maintenance, part replacements or design additions. A useful feature of the device would be an automated calibration process where the robot and imaging software could be linked, allowing the robot and scanner to work in tandem to perform calibration imaging as the robot moves to preset positions. Since this would likely take a few hours, the device could be left to perform this procedure automatically overnight, when there is less demand for the MR scanner.

## 4.4 Final Remarks

As preclinical models and preclinical MR imaging continue to develop, the need for highly accurate surgical tools to perform minimally invasive local injections will increase, just as it has in human applications. The combination of exceptional soft tissue MR imaging and high robotic targeting accuracy have proven to be a powerful pair in accurately delivering needles to specific targets in soft tissues, and has opened opportunities for various minimally invasive MR image-guided surgical applications. Although this device is still in development, the testing of the proof-

of-concept device was successful and has hopefully helped pave the way for future MR image-guided procedures to improve the standard quality of research.

# References

1. European Commission. *Seventh Report on the Statistics on the Number of Animals Used for Experimental and Other Scientific Purposes in the Member States of the European Union.*; 2013.
2. United States Department of Agriculture - Animal and Health Inspection Services. Annual report animal usage by fiscal year. 2015:10.
3. Church DM, Goodstadt L, Hillier LW, et al. Lineage-specific biology revealed by a finished genome assembly of the mouse. *PLoS Biol.* 2009;7(5). doi:10.1371/journal.pbio.1000112.
4. Doyle A, McGarry MP, Lee NA, Lee JJ. The Construction of Transgenic and Gene Knockout/Knockin Mouse Models of Human Disease. *Transgenic Res.* 2013;21(2):327-349. doi:10.1007/s11248-011-9537-3.The.
5. Politi K, Pao W. How genetically engineered mouse tumor models provide insights into human cancers. *J Clin Oncol.* 2011;29(16):2273-2281. doi:10.1200/JCO.2010.30.8304.
6. Picciotto MR, Wickman K. Using knockout and transgenic mice to study neurophysiology and behavior. *Physiol Rev.* 1998;78(4):1131-1163.
7. Elder GA, Gama Sosa MA, De Gasperi R. Transgenic Mouse Models of Alzheimer's Disease. *Mt Sinai J Med A J Transl Pers Med.* 2010;77(1):69-81. doi:10.1002/msj.20159.
8. Shibata N. Transgenic mouse model for familial amyotrophic lateral sclerosis with superoxide dismutase-1 mutation. *Neuropathology.* 2001;21(1):82-92.
9. Pritchard JF, Jurima-Romet M, Reimer MLJ, Mortimer E, Rolfe B, Cayen MN. Making better drugs: Decision gates in non-clinical drug development. *Nat Rev Drug Discov.* 2003;2(7):542-553. doi:10.1038/nrd1131.
10. Zambrowicz BP, Sands AT. Knockouts model the 100 best-selling drugs--will they model the next 100? *Nat Rev Drug Discov.* 2003;2(1):38-51. doi:10.1038/nrd987.
11. Zhang L, Xu X, Hu C, et al. A High-Frequency High Frame Rate Duplex Ultrasound Linear Array Imaging System for Small Animal Imaging. *IEEE Trans Ultrason Ferroelectr Freq Control.* 2010;57(7):1548-1557. doi:10.1109/TUFFC.2010.1585.
12. Shung KK. High Frequency Ultrasonic Imaging. *J Med Ultrasound.* 2009;17(1):25-30. doi:10.1016/S0929-6441(09)60012-6.
13. Bax JS, Waring CSR, Sherebrin S, et al. 3D image-guided robotic needle positioning system for small animal interventions. *Med Phys.* 2013;40(1):- . doi:http://dx.doi.org/10.1118/1.4771958.
14. Badea C, M D, Holdsworth D, Johnson G, Angiography S. In vivo small animal imaging using micro-CT and digital subtraction angiography. *Phys Med Biol.* 2008;53(19):1-36. doi:10.1088/0031-9155/53/19/R01.In.
15. Duyn JH. The future of ultra-high field MRI and fMRI for study of the human brain. *Neuroimage.* 2012;62(2):1241-1248. doi:10.1016/j.neuroimage.2011.10.065.
16. Huettel SA, Song AW, McCarthy G. Functional magnetic resonance imaging. 2004.



17. Krupnick AS, Lin X, Li W, et al. Orthotopic mouse lung transplantation as experimental methodology to study transplant and tumor biology. *Nat Protoc.* 2008;4(1):86-93. <http://dx.doi.org/10.1038/nprot.2008.218>.
18. Vertuani S, Nilsson J, Borgman B, et al. A Cost-Effectiveness Analysis of Minimally Invasive versus Open Surgery Techniques for Lumbar Spinal Fusion in Italy and the United Kingdom. *Value Heal.* 2015;18(6):810-816. doi:10.1016/j.jval.2015.05.002.
19. Starkweather AR, Witek-Janusek L, Nockels RP, Peterson J, Mathews HL. The multiple benefits of minimally invasive spinal surgery: results comparing transforaminal lumbar interbody fusion and posterior lumbar fusion. *J Neurosci Nurs.* 2008;40(1):32-39. doi:10.1097/01376517-200802000-00006.
20. Blair-Handon R, Mueller K, Hoogstraten-Miller S. An alternative method for intrathymic injections in mice. *Lab Anim (NY).* 2010;39(8):248-252. doi:10.1038/labam0810-248.
21. Springer ML, Sievers RE, Viswanathan MN, et al. Closed-chest cell injections into mouse myocardium guided by high-resolution echocardiography. *Am J Physiol Heart Circ Physiol.* 2005;289(3):H1307-H1314. doi:10.1152/ajpheart.00164.2005.
22. Sharief AA, Badea A, Dale AM, Johnson GA. Automated segmentation of the actively stained mouse brain using multi-spectral MR microscopy. *Neuroimage.* 2008;39(1):136-145. doi:10.1016/j.neuroimage.2007.08.028.
23. Chen XJ, Kovacevic N, Lobaugh NJ, Sled JG, Henkelman RM, Henderson JT. Neuroanatomical differences between mouse strains as shown by high-resolution 3D MRI. *Neuroimage.* 2006;29(1):99-105. doi:10.1016/j.neuroimage.2005.07.008.
24. Wahlsten D, Hudspeth WJ, Bernhardt K. Implications of genetic variation in mouse brain structure for electrode placement by stereotaxic surgery. *J Comp Neurol.* 1975;162(4):519-531. doi:10.1002/cne.901620408.
25. Li X, Aggarwal M, Hsu J, Jiang H, Mori S. AtlasGuide: Software for stereotaxic guidance using 3D CT/MRI hybrid atlases of developing mouse brains. *J Neurosci Methods.* 2013;220(1):75-84. doi:10.1016/j.jneumeth.2013.08.017.
26. Aggarwal M, Zhang J, Miller MI, Sidman RL, Mori S. Magnetic resonance imaging and micro-computed tomography combined atlas of developing and adult mouse brains for stereotaxic surgery. *Neuroscience.* 2009;162(4):1339-1350. doi:10.1016/j.neuroscience.2009.05.070.
27. Tuckett AZ, Zakrzewski JL, Li D, van den Brink MRM, Thornton RH. Free-hand ultrasound guidance permits safe and efficient minimally invasive intrathymic injections in both young and aged mice. *Ultrasound Med Biol.* 2015;41(4):1105-1111. doi:10.1016/j.ultrasmedbio.2014.11.011.
28. Magnin R, Rabusseau F, Salabartan F, et al. Magnetic resonance-guided motorized transcranial ultrasound system for blood-brain barrier permeabilization along arbitrary trajectories in rodents. *J Ther Ultrasound.* 2015;3(1):22. doi:10.1186/s40349-015-0044-5.
29. Blanco RT, Ojala R, Kariniemi J, Perälä J, Niinimäki J, Tervonen O. Interventional and intraoperative MRI at low field scanner - A review. *Eur J Radiol.* 2005;56(2):130-142. doi:10.1016/j.ejrad.2005.03.033.
30. Cuschieri A. Nature of Human Error. 2006;244(5):642-648. doi:10.1097/01.sla.0000243601.36582.18.

31. Greer AD, Newhook PM, Sutherland GR. Human-machine interface for robotic surgery and stereotaxy. *IEEE/ASME Trans Mechatronics*. 2008;13(3):355-361. doi:10.1109/TMECH.2008.924118.
32. Sutherland G, Maddahi Y, Zareinia K, Gan L, Lama S. Robotics in the neurosurgical treatment of glioma. *Surg Neurol Int*. 2015;6(2):1. doi:10.4103/2152-7806.151321.
33. Waspe AC, Lacefield JC, Fenster A. Registration of Three-Dimensional High-Frequency Ultrasound Images to a Robotic Needle-Positioning System for Pre-Clinical Research. *Biomed Imaging From Nano to Macro, 2007 ISBI 2007 4th IEEE Int Symp*. 2007:1132-1135. doi:10.1109/ISBI.2007.357056.
34. Waspe AC, McErlain DD, Pitelka V, Holdsworth DW, Lacefield JC, Fenster A. Integration and evaluation of a needle-positioning robot with volumetric microcomputed tomography image guidance for small animal stereotactic interventions. *Med Phys*. 2010;37(4):1647. doi:10.1118/1.3312520.
35. Waspe AC, Lacefield JC, Holdsworth DW, Fenster A. Registration of a needle-positioning robot to high-resolution 3D ultrasound and computed tomography for image-guided interventions in small animals. *Proc SPIE*. 2008;6918(September 2015):691807-691807 - 12. doi:10.1117/12.770449.
36. Cepek J, Lindner U, Ghai S, et al. Mechatronic system for in-bore MRI-guided insertion of needles to the prostate: An in vivo needle guidance accuracy study. *J Magn Reson Imaging*. 2014;42(1):48-55. doi:10.1002/jmri.24742.
37. Wilson E, Chiodo C, Wong KH, Fricke S, Jung M, Cleary K. Robotically assisted small animal MRI-guided mouse biopsy. In: Vol 7625. ; 2010:762520-762528. <http://dx.doi.org/10.1117/12.845566>.
38. Hynynen K, McDannold N, Vykhodtseva N, Jolesz FA. Noninvasive MR Imaging-guided Focal Opening of the Blood-Brain Barrier in Rabbits. *Radiology*. 2001;220(3):640-646. doi:10.1148/radiol.2202001804.
39. Graham KC, Wirtzfeld LA, MacKenzie LT, et al. Three-dimensional High-Frequency Ultrasound Imaging for Longitudinal Evaluation of Liver Metastases in Preclinical Models. *Cancer Res*. 2005;65(12):5231-5237. doi:65/12/5231 [pii]r10.1158/0008-5472.CAN-05-0440.
40. Serwer L, Hashizume R, Ozawa T, James CD. Systemic and local drug delivery for treating diseases of the central nervous system in rodent models. *J Vis Exp*. 2010;(42):5-9. doi:10.3791/1992.
41. Costa ALF, Appenzeller S, Yasuda CL, Pereira FR, Zanardi VA, Cendes F. Artifacts in brain magnetic resonance imaging due to metallic dental objects. *Med Oral Patol Oral Cir Bucal*. 2009;14(6):278-282.
42. Hargreaves BA, Worters PW, Pauly KB, Pauly JM, Koch KM, Gold GE. Metal-induced artifacts in MRI. *Am J Roentgenol*. 2011;197(3):547-555. doi:10.2214/AJR.11.7364.
43. Koch KM, Hargreaves B a, Pauly KB, Chen W, Gold GE, King KF. Magnetic resonance imaging near metal implants. *J Magn Reson Imaging*. 2010;32(4):773-787. doi:10.1002/jmri.22313.
44. Chen CA, Chen W, Goodman SB, et al. New MR Imaging Methods for Metallic Implants in the Knee: Artifact Correction and Clinical Impact. *J Magn Reson Imaging*. 2011;33(5):1121-1127. doi:10.1002/jmri.22534.

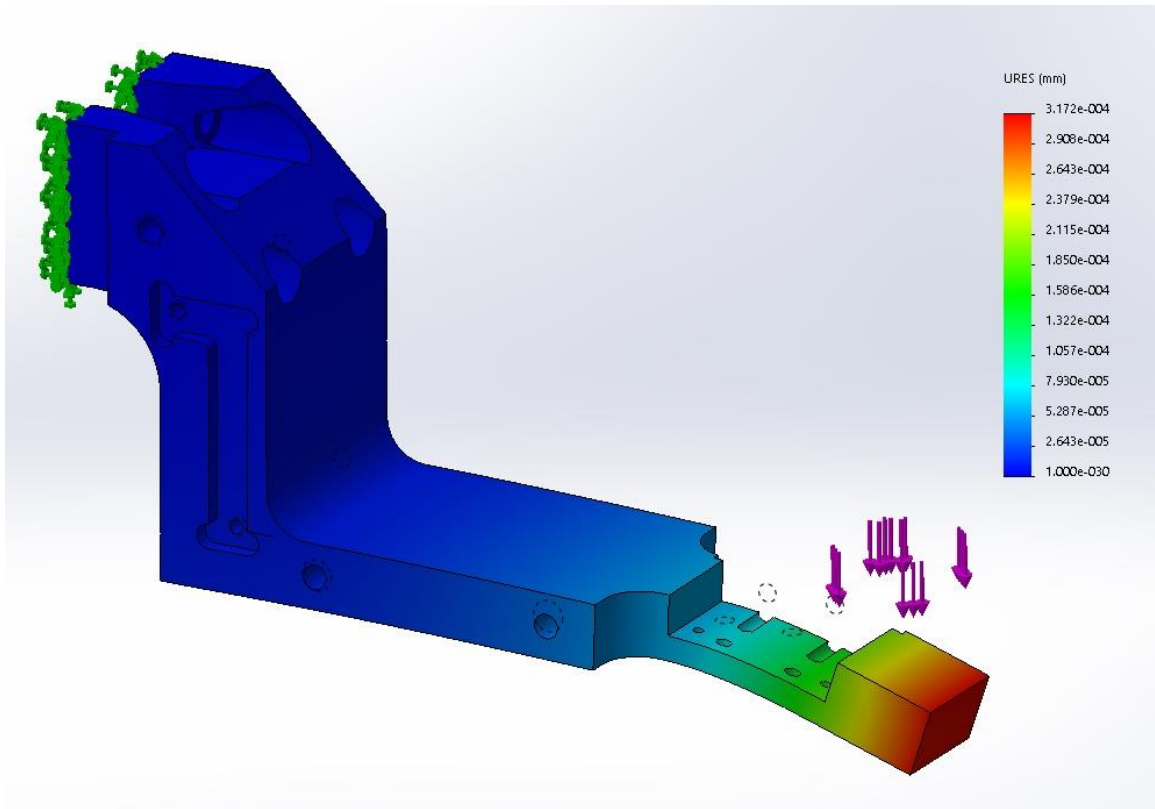
45. Calisaneller T, Lin C-L, Ukita N, et al. Animal Models of Acute Neurological Injuries. In: Chen J, Xu ZC, Xu X-M, Zhang JH, eds. Totowa, NJ: Humana Press; 2009:287-292. doi:10.1007/978-1-60327-185-1\_24.
46. Altay T, Smithason S, Volokh N, Rasmussen PA, Ransohoff RM, Provencio JJ. A novel method for subarachnoid hemorrhage to induce vasospasm in mice. *J Neurosci Methods*. 2009;183(2):136-140. doi:10.1016/j.jneumeth.2009.06.027.
47. Waspe AC, Cakiroglu HJ, Lacefield JC, Fenster A. Design and Validation of a Robotic Needle Positioning System for Small Animal Imaging Applications. *Eng Med Biol Soc 2006 EMBS '06 28th Annu Int Conf IEEE*. 2006:412-415. doi:10.1109/IEMBS.2006.260206.
48. Yang B, Roys S, Tan U-X, et al. Design, Development, and Evaluation of a Master-Slave Surgical System for Breast Biopsy under Continuous MRI(). *Int J Rob Res*. 2014;33(4):616-630. doi:10.1177/0278364913500365.
49. Moche M, Zajonz D, Kahn T, Busse H. MRI-guided procedures in various regions of the body using a robotic assistance system in a closed-bore scanner: Preliminary clinical experience and limitations. *J Magn Reson Imaging*. 2010;31(4):964-974. doi:10.1002/jmri.21990.
50. Kokes R, Lister K, Gullapalli R, et al. Towards a teleoperated needle driver robot with haptic feedback for RFA of breast tumors under continuous MRI. *Med Image Anal*. 2009;13(3):445-455. doi:10.1016/j.media.2009.02.001.
51. Wang Y, Cole G a., Su H, Pilitsis JG, Fischer GS. MRI compatibility evaluation of a piezoelectric actuator system for a neural interventional robot. *Proc 31st Annu Int Conf IEEE Eng Med Biol Soc Eng Futur Biomed EMBC 2009*. 2009:6072-6075. doi:10.1109/IEMBS.2009.5334206.
52. Lang MJ, Greer AD, Sutherland GR. Intra-operative robotics: NeuroArm. *Acta Neurochir Suppl*. 2011;109:231-236. doi:10.1007/978-3-211-99651-5.
53. Waspe AC, Cakiroglu HJ, Lacefield JC, Fenster A. Design and validation of a robotic needle positioning system for small animal imaging applications. *Annu Int Conf IEEE Eng Med Biol - Proc*. 2006;1863:412-415. doi:10.1109/IEMBS.2006.260206.
54. Cepek J, Chronik B a, Lindner U, et al. A system for MRI-guided transperineal delivery of needles to the prostate for focal therapy. *Med Phys*. 2013;40(1):012304. doi:10.1118/1.4773043.
55. Cepek J, Chronik BA, Fenster A. The effects of magnetic field distortion on the accuracy of passive device localization frames in MR imaging. *Med Phys*. 2014;41(5).
56. Tator CH, Day a., Ng R, Liberman L. Chemotherapy of an experimental glioma with nitrosoureas. *Cancer Res*. 1977;37(2):476-481.
57. Krause S, Brock A, Ingber DE. Intraductal Injection for Localized Drug Delivery to the Mouse Mammary Gland. *J Vis Exp*. 2013;(80):1-5. doi:10.3791/50692.
58. El-Ghamari M, Bergmann F, Schmied BM, Weitz J, Ulrich A. Islet cells contribute to pancreatic carcinogenesis in an animal model. *Pancreas*. 2011;40(2):242-246. doi:10.1097/MPA.0b013e3182016a08.
59. Carbajal KS, Weinger JG, Whitman LM, Schaumburg CS, Lane TE. Surgical Transplantation of Mouse Neural Stem Cells into the Spinal Cords of Mice Infected with

- Neurotropic Mouse Hepatitis Virus. *J Vis Exp*. 2011;9(53):3-7. doi:10.3791/2834.
60. Adjali O, Marodon G, Steinberg M, et al. In vivo correction of ZAP-70 immunodeficiency by intrathymic gene transfer. *J Clin Invest*. 2005;115(8):2287-2295. doi:10.1172/JCI23966.
  61. Inquimbert P, Moll M, Kohno T, Scholz J. Stereotaxic Injection of a Viral Vector for Conditional Gene Manipulation in the Mouse Spinal Cord. *J Vis Exp*. 2013;(73):1-5. doi:10.3791/50313.
  62. Foust KD, Kaspar BK. Over the barrier and through the blood; To CNS delivery we go. *Cell Cycle*. 2009;8(24):4017-4018. <http://www.ncbi.nlm.nih.gov/pmc/articles/PMC2911437/>.
  63. Cayrol R, Haqqani AS, Ifergan I, Dodelet-Devillers A, Prat A. Isolation of human brain endothelial cells and characterization of lipid raft-associated proteins by mass spectroscopy. *Methods Mol Biol*. 2011;686(1):275-295. doi:10.1007/978-1-60761-938-3.
  64. Messier C, Émond S, Ethier K. New techniques in stereotaxic surgery and anesthesia in the mouse. *Pharmacol Biochem Behav*. 1999;63(2):313-318. doi:10.1016/S0091-3057(98)00247-0.
  65. Jones GB, Wahlsten D, Blom G. Precision stereotaxic procedure for the mouse (*Mus musculus*): Method and instrumentation. *Physiol Behav*. 1977;19(3):445-448. doi:10.1016/0031-9384(77)90294-3.
  66. Jones BGB, Wahlsten D, Blom G. Precision Stereotaxic Procedure for the Mouse (*Mus musculus*): Method and Instrumentation. *Physiol Behav*. 1977:445-448.
  67. Aime S, Caravan P. Biodistribution of gadolinium-based contrast agents, including gadolinium deposition. *J Magn Reson Imaging*. 2009;30(6):1259-1267. doi:10.1002/jmri.21969.
  68. Markiewicz E, Fan X, Mustafi D, et al. High resolution 3D MRI of mouse mammary glands with intra-ductal injection of contrast media. *Magn Reson Imaging*. August 2014. doi:10.1016/j.mri.2014.08.035.
  69. Shahbazi-Gahrouei D. Novel MR imaging contrast agents for cancer detection. *J Res Med Sci*. 2009;14(3):141-147. <http://www.ncbi.nlm.nih.gov/pmc/articles/PMC3129053/>.
  70. Pérez-Rivera A a, Fink GD, Galligan JJ. Increased reactivity of murine mesenteric veins to adrenergic agonists: functional evidence supporting increased alpha1-adrenoceptor reserve in veins compared with arteries. *J Pharmacol Exp Ther*. 2004;308(1):350-357. doi:10.1124/jpet.103.056184.1970.
  71. Graham KC. Three-dimensional High-Frequency Ultrasound Imaging for Longitudinal Evaluation of Liver Metastases in Preclinical Models. *Cancer Res*. 2005;65(12):5231-5237. doi:10.1158/0008-5472.CAN-05-0440.
  72. Melzer A, Gutmann B, Remmele T, et al. INNOMOTION for percutaneous image-guided interventions. *IEEE Eng Med Biol Mag*. 2008;27(3):66-73. doi:10.1109/EMB.2007.910274.
  73. Schouten MG, Bomers JGR, Yakar D, et al. Evaluation of a robotic technique for transrectal MRI-guided prostate biopsies. *Eur Radiol*. 2012;22(2):476-483. doi:10.1007/s00330-011-2259-3.

74. Sharp AA, Ortega AM, Restrepo D, Curran-Everett D, Gall K. In Vivo Penetration Mechanics and Mechanical Properties of Mouse Brain Tissue at Micrometer Scales. *Biomed Eng IEEE Trans.* 2009;56(1):45-53. doi:10.1109/TBME.2008.2003261.
75. The MathWorks Inc. MATLAB Image Processing Toolbox (R2014b). <http://www.mathworks.com/products/image/>.
76. Chang H, Fitzpatrick JM. A Technique for Accurate Magnetic Resonance Imaging in the Presence of Field Inhomogeneities. *IEEE Trans Med Imaging.* 1992;11(3):319-329. doi:10.1109/42.158935.
77. Surry KJM, Austin HJB, Fenster A, Peters TM. Poly (vinyl alcohol) cryogel phantoms for use in ultrasound and MR imaging. *Phys Med Biol.* 2004;49(24):5529. doi:10.1088/0031-9155/49/24/009.
78. Yamazaki Y, Hirai Y, Miyake K, Shimada T. Targeted gene transfer into ependymal cells through intraventricular injection of AAV1 vector and long-term enzyme replacement via the CSF. *Sci Rep.* 2014;4:5506. doi:10.1038/srep05506.

# Appendix

## Appendix 1



The resultant displacement of the mouse bed from the Solidworks FEA Simulation shows a maximum needle induced deflection of  $0.3\mu\text{m}$  from an applied force of  $3\text{mN}$ . The color scale depicts the URES “displacement resultant” which is predominantly in the vertical direction. The green arrows on the left of the mouse bed represent the fixed surface, which is not visible from this angle, while the purple arrows represent the vertical force applied to the end of the mouse bed by the needle in a worst case scenario, as described in Section 2.3.3. This FEA only accounts for the dominant mouse bed deflection, although there are other sources of deflection in the XYZ-stage.

# Curriculum Vitae

Name: Matthew James Gravett

## EDUCATION

- 2013-2016                    **University of Western Ontario**, London, Ontario, Canada  
Master of Engineering Science (M.E.Sc.)  
Biomedical Engineering Graduate Program
- 2009-2013                    **Queen's University**, Kingston, Ontario, Canada  
Bachelor of Science Engineering (B.Sc.)  
Mechanical Engineering (Biomechanics)

## INDUSTRIAL EXPERIENCE

- 5/2013 - 8/2013            **Center for Imaging Technology Commercialization (CIMTEC)**,  
London, Ontario, Canada  
Mechanical Design  
Summer Student (Full-Time)
- 5/2012 - 8/2012            **Center for Imaging Technology Commercialization (CIMTEC)**,  
London, Ontario, Canada  
Mechanical Design  
Summer Student (Full-Time)

## RESEARCH EXPERIENCE

- 9/2012 - 4/2013            **Cardiovascular Imaging Network at Queen's (CINQ)**, Kingston,  
Ontario, Canada  
Medical Imaging  
Volunteer Research Assistant (Part-Time)
- 5/2011 - 8/2011            **Robarts Research Institute**, London, Ontario, Canada  
Medical Imaging  
Mechanical Engineering Summer Student (Full-Time)
- 5/2010 - 8/2010            **Robarts Research Institute**, London, Ontario, Canada  
Medical Imaging  
Mechanical Engineering Summer Student (Full-Time)

## TEACHING EXPERIENCE

- Winter 2014/15            **University of Western Ontario**  
ENGSCI 2211G: Engineering Communications  
Graduate Teaching Assistant, 70 hours (2014), 105 hours (2015)
- Fall 2013/14                **University of Western Ontario**  
MEDBIO 4535A: Hemodynamics  
Graduate Teaching Assistant, 70 hours

## **SCHOLARSHIPS**

9/2013 – 8/2015      **Western Graduate Research Scholarship (\$16 000)**  
University of Western Ontario

5/2014 – 4/2015      **Ontario Graduate Scholarship (\$15 000)**  
University of Western Ontario

## **AWARDS**

3/2015                      **Imaging Network Ontario (\$100)**  
Ontario Institute for Cancer Research Imaging Translation Program  
Consortium

4/2013                      **George Christie Design Award (\$125)**  
Queen's University

## **PUBLICATIONS**

Amer M. Johri, David W. Chitty, Murray Matangi, Paul Malik, Parvin Mousavi, Andrew Day, Matthew Gravett, Chris Simpson. "Can Carotid Bulb Plaque Assessment Rule Out Significant Coronary Artery Disease? A Comparison of Plaque Quantification by Two- and Three-Dimensional Ultrasound", Journal of the American Society of Echocardiography, Volume 26, Issue 1, January 2013, Pages 86-95, ISSN 0894-7317.